

VEGAS: a VST Early-type GALaxy Survey

V. IC 1459 group: Mass assembly history in low density environments

Enrichetta Iodice^{1,2}, Marilena Spavone¹, Arianna Cattapan¹, Elena Bannikova^{3,4}, Duncan A. Forbes⁵, Roberto Rampazzo⁶, Stefano Ciroi^{7,8}, Enrico Maria Corsini^{7,8}, Giuseppe D'Ago⁹, Tom Oosterloo^{10,11}, Pietro Schipani¹, and Massimo Capaccioli¹²

¹ INAF – Astronomical Observatory of Capodimonte, Salita Moiariello 16, I-80131, Naples, Italy

e-mail: enrichetta.iodice@inaf.it

² European Southern Observatory, Karl-Schwarzschild-Strasse 2, D-85748 Garching bei Muenchen, Germany

³ Institute of Radio Astronomy of National Academy of Sciences of Ukraine, Mystetstv 4, UA-61022 Kharkiv, Ukraine

⁴ V. N. Karazin Kharkiv National University, Svobody Sq. 4, UA-61022 Kharkiv, Ukraine

⁵ Centre for Astrophysics and Supercomputing, Swinburne University of Technology, Hawthorn, Victoria 3122, Australia

⁶ INAF – Astronomical Observatory of Padova, Via dell'Osservatorio 8, I-36012, Asiago (VI), Italy

⁷ Department of Physics and Astronomy "G. Galilei", University of Padova, Vicolo dell'Osservatorio 3, I-35122, Padova, Italy

⁸ INAF – Osservatorio Astronomico di Padova, Vicolo dell'Osservatorio 5, I-35122 Padova, Italy

⁹ Instituto de Astrofísica, Facultad de Física, Pontificia Universidad Católica de Chile, Av. Vicuña Mackenna 4860, 7820436 Macul, Santiago, Chile

¹⁰ ASTRON, Netherlands Institute for Radio Astronomy, Postbus 2, 7990 AA Dwingeloo, The Netherlands

¹¹ Kapteyn Astronomical Institute, University of Groningen, Postbus 800, 9700 AV Groningen, The Netherlands

¹² University of Naples Federico II, C.U. Monte Sant'Angelo, via Cinthia, I-80126, Naples, Italy

Received ???; accepted ???

ABSTRACT

Context. This paper is based on the multi-band VST Early-type GALaxy Survey (VEGAS) with the VLT Survey Telescope (VST). We present new deep photometry of the IC 1459 group in *g* and *r* band.

Aims. The main goal of this work is to investigate the photometric properties of the IC 1459 group, and to compare our results with those obtained for other galaxy groups studied in VEGAS, in order to provide a first view of the variation of their properties as a function of the evolution of the system.

Methods. For all galaxies in the IC 1459 group, we fit isophotes and extract the azimuthally-averaged surface-brightness profiles, the position angle and ellipticity profiles as a function of the semi-major axis, as well as the average colour profile. In each band, we estimate the total magnitudes, effective radii, mean colour, and total stellar mass for each galaxies in the group. Then we look at the structure of the brightest galaxies and faint features in their outskirts, considering also the intragroup component.

Results. The wide field of view, long integration time, high angular resolution, and arcsec-level seeing of OmegaCAM@VST allow us to map the light distribution of IC 1459 down to a surface brightness level of $29.26 \text{ mag arcsec}^{-2}$ in *g* band and $28.85 \text{ mag arcsec}^{-2}$ in *r* band, and out to $7 - 10 R_e$, and to detect the optical counterpart of HI gas around IC 1459. We also explore in depth three low density environments and provide information to understand how galaxies and groups properties change with the group evolution stage.

Conclusions. There is a good agreement of our results with predictions of numerical simulations regarding the structural properties of the brightest galaxies of the groups. We suggest that the structure of the outer envelope of the BCGs (i.e. the signatures of past mergers and tidal interactions), the intra-group light and the HI amount and distribution may be used as indicators of the different evolutionary stage and mass assembly in galaxy groups.

Key words. Survey – Galaxies: photometry – Galaxies: elliptical and lenticular, cD – Galaxies: fundamental parameters – Galaxies: groups: individual: IC 1459 group

1. Introduction

The hierarchical accretion scenario is one of the main products of the Λ CDM model, with structures forming as the result of merging of smaller elements (De Lucia et al. 2006). In this framework, at a first epoch the galaxies lie along cosmic web filaments, then due to gravity they fall into small galaxy groups, and these low density environments merge into galaxy clusters (Rudick et al. 2009; Mihos 2015). These small-size environments contain more than $\sim 60\%$ of the galaxies in the Universe, and here galaxies spend a meaningful part of their evolutionary

life (Miles et al. 2004). According to Bower & Balogh (2004), in the local universe, the difference between groups and cluster of galaxies is based on the virial mass: a group of galaxies it is in the range $10^{13} - 10^{14} M_{\odot}$.

During the infall of galaxy groups to form a cluster, the material stripped from galaxy outskirts builds up the intra-group light (IGL) and intra-cluster light (ICL, Fujita 2004; Willman et al. 2004; Contini et al. 2014; DeMaio et al. 2018). The IGL is the precursor of the ICL (Mihos 2015). Since ICL/IGL is the fossil record of all past interactions and mergers, the con-

stant evolution and growth of the ICL/IGL over time with the infalling of galaxies in the potential well of the brightest cluster/group galaxy (BCG/BGG), suggests that the ICL/IGL properties should be linked to the evolutionary state of the cluster/group (Mihos 2015). In this process, the mass assembly in the BCG/BGG is still on-going. The imprint of mass assembly in the BCGs/BGGs resides in the stellar halo. This is an extended, diffuse, and very faint ($\mu_g \geq 26-27$ mag/arcsec²) component made of stars stripped from satellite galaxies, in the form of streams and tidal tails, with multiple stellar components and complex kinematics (see Duc 2017; Mihos et al. 2017, for reviews). Recent theoretical works provide a detailed set of simulations to reproduce the faint features in the galaxy outskirts at comparable levels of the deep observations (i.e. 29-33 mag/arcsec², Pop et al. 2018; Mancillas et al. 2019). They made a census of the various types of low surface brightness (LSB) features and traced their evolution. According to Mancillas et al. (2019), the tidal tails are thick elongated structures that emerge from the parent galaxy. Differently, the stellar streams are tiny filamentary features that originates from the disruption of low-mass satellites in the galaxy halo. Shells have arc-like concentric shapes and, depending on the nature and projection, they can appear aligned on the same axis. Tidal tails and shells in the galaxy outskirts results from intermediate and major mergers (mass ratio 7:1 to 3:1), whereas the stellar streams are typical signatures of minor-mergers. The survival time is estimated between 0.7 up to 4 Gyr, where tidal tails have the shorter life time with respect to shells and streams.

Semi-analytic models combined with simulations give detailed predictions about the structure and stellar populations of stellar halos, the ICL/IGL formation and the amount of sub-structures in various kinds of environment (Oser et al. 2010; Cooper et al. 2013, 2015; Cook et al. 2016; Pillepich et al. 2018; Monachesi et al. 2019). Predictions cited above suggest that the BCGs/BGGs have an inner stellar component formed *in-situ*, whereas the accreted *ex-situ* component contains all the accreted material. The *ex-situ* component is made by the relaxed component, which is completely merged with the *in-situ* component, and by the un-relaxed component, which is the outer stellar envelope. Simulations show that in the surface-brightness radial profile of simulated galaxies there is evidence of *inflection* in the region of the stellar halos, corresponding to variations in the ratio between the accreted relaxed and the accreted un-relaxed components (Cooper et al. 2010; Deason et al. 2013; Amorisco 2017). This distance from the galaxy centre where the inflection occurs is the *transition radius* (R_{tr}) used to characterise stellar halo. Massive galaxies with an high accreted mass fraction have a small R_{tr} (Cooper et al. 2010, 2013). The un-relaxed component of the stellar envelope appears as a change in the slope at larger radii of the surface brightness profiles. In this context, the study of the surface brightness profiles of BCG/BGG at the faintest levels is potentially one of the main "tools" to quantify the contribution of the accreted mass, which becomes particularly efficient when the outer stellar envelope starts to be dominant beyond the transition radius (Iodice et al. 2016, 2017b; Spavone et al. 2017a, 2018).

In the last two decades, a huge enhancement to the study of BCGs/BGGs and on the ICL in different type of environments has been given by deep imaging surveys aimed at studying galaxy structures out to the regions where the galaxy light merges into the intra-cluster component (Ferrarese et al. 2012; van Dokkum et al. 2014; Duc et al. 2015; Muñoz et al. 2015; Merritt et al. 2016; Mihos et al. 2017). The *VST Early-type*

Galaxy Survey (VEGAS¹, Capaccioli et al. 2015) has occupied in the last years a pivotal role in this field. VEGAS is a multi-band *ugri* imaging survey with the VLT Survey Telescope (VST). Taking advantage of the large field-of-view of OmegaCAM@VST, VEGAS data allow to relate the galaxy structure with environment, from the dense cluster of galaxies (see Iodice et al. 2019, and reference therein) to the unexplored poor groups of galaxies (Spavone et al. 2018; Cattapan et al. 2019). With the VEGAS data we are able to map the surface brightness of galaxies down to $\mu_g \sim 30$ mag/arcsec² and out to about $10R_e$ (Spavone et al. 2017a; Iodice et al. 2019). The deep photometry allows to trace the mass assembly in galaxies, by estimating the accreted mass fraction in the stellar halos, detecting the ICL and the stellar streams in the intra-cluster space, and providing results that can be directly compared with the predictions of galaxy formation models (Iodice et al. 2016, 2017a,b; Spavone et al. 2017a, 2018; Cattapan et al. 2019). Recently, in the deep imaging data of VEGAS for the NGC 5846 group of galaxies, we were able to detect an ultra diffuse galaxy, with an absolute magnitude of $M_g = -14.2$ mag, corresponding to a stellar mass of $\sim 10^8 M_\odot$ (Forbes et al. 2019).

In this work we present a new VEGAS deep mosaic of 1×2 square degrees of the group of galaxies centred on the BGG IC 1459. We use *g*, *r*, and *i* images to analyse the structure of the group members, to detect any LSB features in the BGG outskirts and in the intra-group space. Results are compared with those obtained for other two galaxy groups studied in VEGAS, the NGC 5018 group (Spavone et al. 2018) and NGC 1533 triplet (Cattapan et al. 2019), since data have comparable depth and were analysed using the same methods and tools.

The paper is organised as follow. In Section 2 we describe the IC 1459 group and its main properties. The observing strategy and the data reduction procedure are reported in Section 3. In Section 4 we present the data analysis and in Section 5 we describe the results for the IC 1459 group. In Section 6 we compare the results of the three analysed VEGAS groups with theoretical predictions and with previous observational results. In Section 7 we draw our conclusions.

2. The IC 1459 Group

The IC 1459 group (also known as LGG 466) hosts 9 bright galaxies, of which 7 are LTGs (Brough et al. 2006). IC 1459 is an ETG located in the group projected centre and it is considered the BGG of this group (Saponara et al. 2018). By adopting the virial radius given by Brough et al. (2006), $r_{200} = 0.21$ Mpc, we derived the virial mass for the group $M_{200} \simeq 3.7 \times 10^{13} M_\odot$. In this work, we studied the brightest galaxies in the range of magnitude $-23 \leq M_g \leq 19.6$ mag. IC 1459 is one of the two ETGs of the group. It is the most massive, $M_{tot}^* = 1.0 \times 10^{12} M_\odot$, and luminous, $L_{tot,g} = 1.77 \times 10^{11} L_\odot$, galaxy. Table 1 lists the main properties of the galaxies in the IC 1459 group and Figure 1 shows the OmegaCAM@VST mosaic in *g* band of the group. We consider each of the group members at the same distance of IC 1459, $D = 28.70$ Mpc, based on the HI data (Brough et al. 2006; Serra et al. 2015; Saponara et al. 2018; Oosterloo et al. 2018).

In the last decades, the entire group centred on IC 1459 was well studied in a wide wavelength range. Osmond & Ponman (2004) found X-rays emission from a diffuse intragroup medium. Kilborn et al. (2009), by studying the HI content of the group, pointed out that the gas-rich spirals have typical HI masses,

¹ see <http://www.na.astro.it/vegas/VEGAS/Welcome.html>

Table 1. Basic properties of the galaxies in the IC 1459 group.

Galaxy	Morphological Type	R.A. (J2000)	Decl. (J2000)	Helio.radial velocity km s ⁻¹
IC 1459	E3-4	22 ^h 57 ^m 10 ^s .61	-36°27′44″.0	1802
IC 5269	SAB0(rs):	22 ^h 57 ^m 43 ^s .66	-36°01′34″.4	1967
IC 5269B	SB(rs)cd:	22 ^h 56 ^m 36 ^s .72	-36°14′59″.2	1667
IC 5270	SB(r)cd: (e)	22 ^h 57 ^m 54 ^s .94	-35°51′29″.0	1983
IC 5264	Sab pec (e)n	22 ^h 56 ^m 53 ^s .04	-36°33′15″.0	1934
ESO 406-27	SA(rs)d:	22 ^h 56 ^m 41 ^s .25	-36°46′21″.8	2102
NGC 7418	SAB(rs)cd	22 ^h 56 ^m 36 ^s .16	-37°01′48″.3	1450
NGC 7421	SB(rs)bc	22 ^h 56 ^m 54 ^s .33	-37°20′50″.1	1792
IC 5273	SB(rs)cd:	22 ^h 59 ^m 26 ^s .70	-37°42′10″.4	1293

Notes. Morphological classifications are from RC3, the Third Reference Catalogue of Bright Galaxies (de Vaucouleurs et al. 1991). Coordinates and radial velocities are from NED, the NASA/IPAC Extragalactic Database^a.

^a <https://ned.ipac.caltech.edu>

which suggests that the gas removal mechanisms are not yet activated. Therefore, according to the subsequent analysis by Serra et al. (2015), the HI distribution seems to be consistent with a relatively early stage of group assembly. In contrast, the brightest group member IC 1459 shows clear signs of accretion and/or merging events. First study of the IC 1459 was provided by Malin (1985), using photographic plates, which pointed out the disturbed morphology in the outskirts, in the form of spiral-like features. The morphology of IC 1459 appears quite disturbed by the presence of a dust lane in the centre (Forbes et al. 1994) and by shells, plumes, and faint features in the galaxy outskirts (Forbes et al. 1995). The galaxy hosts an active galactic nucleus with two symmetric radio jets (Tingay & Edwards 2015). Stellar kinematics revealed the existence of a fast counter-rotating stellar core that might result from the accretion of counter-rotating cold gas streams in early times (Franx & Illingworth 1988; Prichard et al. 2019).

3. Observations and Data Reduction

The IC 1459 group is one of the *VEGAS* target (P.I. E. Iodice; Capaccioli et al. 2015). *VEGAS* is a multi-band *u*, *g*, *r* and *i* imaging survey obtained with the European Southern Observatory (ESO) Very Large Telescope Survey Telescope (VST). VST is a 2.6 m wide field optical telescope (Schipani et al. 2012), equipped with OmegaCAM, a 1° × 1° camera with a resolution of 0.21 arcsec pixel⁻¹. The data we present were obtained in visitor mode (run IDs: 097.B-0806(B), 098.B-0208(A) and 0100.B-0168(A)), in dark time. The total integration times and the average FWHM in each band are given in Table 2. A detailed description of the data reduction, using the dedicated pipelines developed to process OmegaCam observations (*VST-Tube* and *AstroWISE*) is provided by McFarland et al. (2013); Grado et al. (2012); Capaccioli et al. (2015); Spavone et al. (2017b); Venhola et al. (2018).

For the IC 1459 group, we have obtained a mosaic of about 1° × 2°, it is shown in Fig. 1. Data were acquired with the *step dither* observing strategy, consisting of a cycle of short exposures (~ 150 sec) on the science target and on an adjacent field (close in space and time) to the science frame. This strategy was adopted for other *VEGAS* targets (as for the NGC 5018 group, Spavone et al. 2018) and for the Fornax Deep Survey (FDS Iodice et al. 2016; Venhola et al. 2018) and it guarantees a very accurate estimate of the sky background, since an average

sky frame was derived for each observing night and then subtracted from each science frame. With the total exposure times adopted for the observations of IC 1459 group, the obtained surface brightness depths for a point source at 5σ over an area of FWHM=1.26 arcsec are $\mu_g = 27.3$ mag, $\mu_r = 28.9$ mag and $\mu_i = 26.2$ mag in the *g*, *r* and *i* band respectively.

By adopting the same method described in Iodice et al. (2016), on the sky-subtracted and stacked images, we estimated any residual fluctuations² and the limiting radius from the galaxy centre where the galaxy’s light blends into the background. In short, for each galaxy of the sample and in each band, we extracted the azimuthally-averaged intensity profile (using the IRAF task ELLIPSE) on the sky-subtracted mosaic, after masking all the bright sources (galaxies and stars) and background objects, and from it we estimated the outermost radius, from the centre of the galaxy, where counts are consistent with the average background level. Such a value is the residual by the subtraction of the sky frame, thus it is very close to zero. The limiting radius sets the surface brightness limit of the VST light profiles and gives an estimate on the accuracy of the sky subtraction. The fluctuations of the background level are on average in the range 0.6 – 1 counts in the *g* and *r* bands, respectively and close to zero counts in the *i* band. The RMS in the background fluctuations, which quantify how good is the sky subtraction, is in the range 0.04 – 0.06 counts. RMS and the uncertainties on the photometric calibration (~ 0.003 – 0.006 mag) are taken into account for computing the total uncertainty on the surface brightness magnitudes³ For IC 1459 the limiting radius is 20 arcmin (~ 167 kpc) in the *g* and *r* bands, and 10 arcmin (~ 83 kpc) in the *i* band. At these radii, we map the surface brightness down to $\mu = 29 \pm 1$ mag/arcsec² in the *g* and *r* bands.

² The “residual fluctuations” in the sky-subtracted images are the deviations from the background in the science frame with respect to the average sky frame obtained by the empty fields close to the target. Therefore, by estimating them, we obtain an estimate on the accuracy of the sky-subtraction step.

³ The uncertainty in the surface brightness is calculated with the following formula: $err = \sqrt{(2.5/(adu \times \ln(10)))^2 \times ((err_{adu} + err_{sky})^2) + err_{zp}^2}$, where $err_{adu} = \sqrt{adu/N - 1}$, with *N* is the number of pixels used in the fit, err_{sky} is the rms on the sky background and err_{zp} is the error on the photometric calibration (Capaccioli et al. 2015; Seigar et al. 2007).

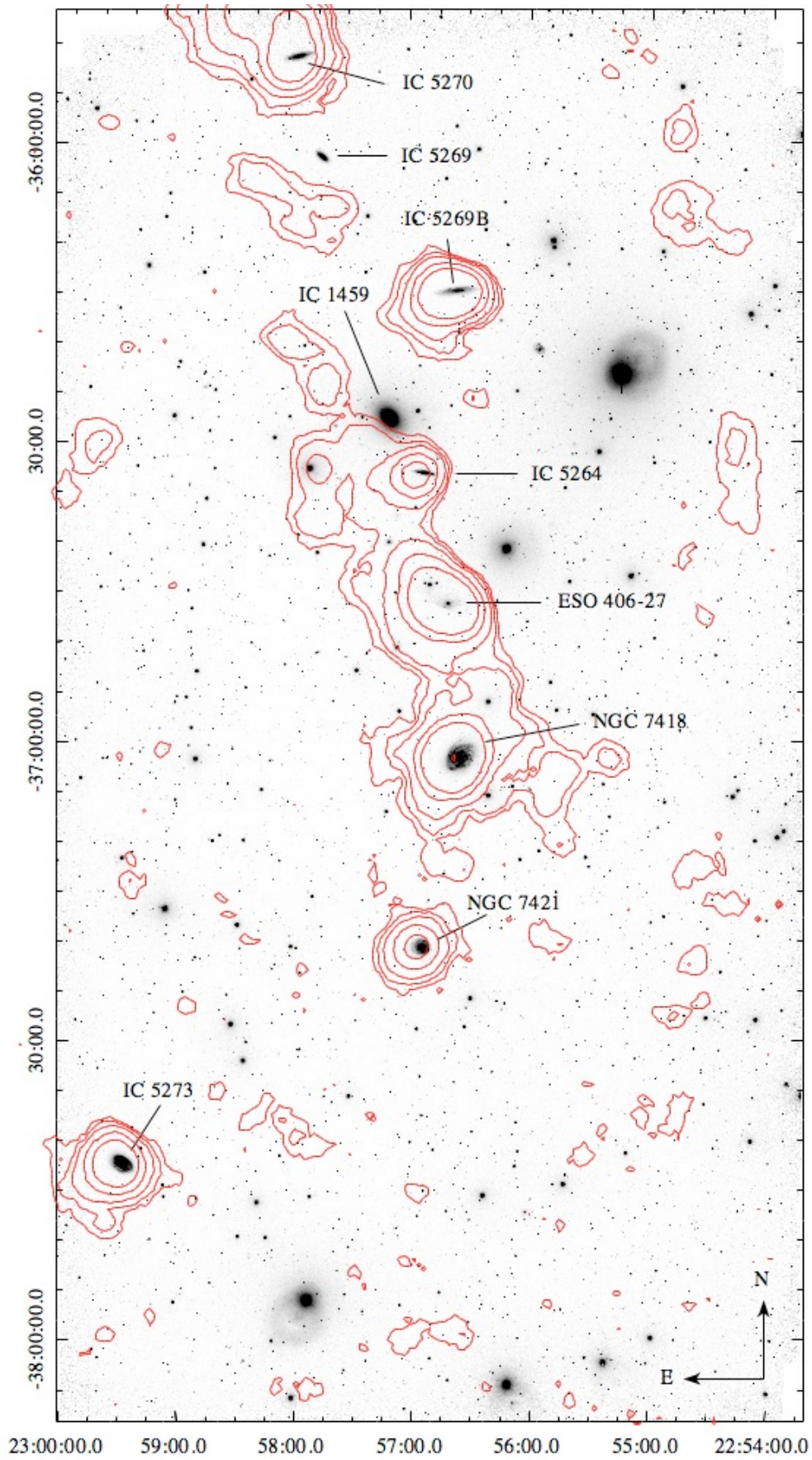


Fig. 1. OmegaCAM@VST mosaic in g band of the IC 1459 group with the HI map from the KAT-7 observations (red contours). The image size is about $1^\circ \times 2^\circ$, and the HI contour levels are $5.5, 10, 20, 50$, and $100 \times 10^{18} \text{ cm}^{-2}$ (as shown by Oosterloo et al. 2018). The right ascension and declination (J2000) are given in the horizontal and vertical axis of the field of view, respectively. The north is at the top and east on the left.

Table 2. Observation log.

Band	RA (J2000)	Decl. (J2000)	T _{exp} (sec)	FWHM (arcsec)
(1)	(2)	(3)	(4)	(5)
<i>g</i>	22 ^h 56 ^m 51 ^s .36	−37°00′50″.4	14250	1.73
<i>r</i>	22 ^h 56 ^m 51 ^s .36	−37°00′50″.4	14400	0.89
<i>i</i>	22 ^h 56 ^m 51 ^s .36	−37°00′50″.4	12750	0.94

Notes. *Col. 1* - filters in the SDSS band; *Col. 2* and *Col. 3* - central right ascension and declination of the mosaic; *Col. 4* - total exposure time; *Col. 5* - median value of the seeing, FWHM, of the combined frames.

To fully account for the broadening effect of the seeing on the light distribution of galaxies, Capaccioli et al. (2015) characterised the point spread function (PSF) for VST by using stars on the acquired VST images. They provided the global PSF surface brightness profile, which takes into account the scattered light out to a radial distance comparable to that of the galaxies' major axis diameter (see Fig. B.1 in Capaccioli et al. 2015). Where needed, a two-dimensional model of the bright stars, close in projection to the galaxy under study, is derived and subtracted off from the image before performing the analysis of the light distribution (see also Sec. 4).

4. Data Analysis

In this section we describe the analysis performed on the new VEGAS data for the IC 1459 group. We provide a detailed description of the galaxy structure at the new faintest surface brightness levels, focusing on the outskirts of the BGG IC 1459. In addition, we derive the *i*) light profiles in all bands and colour distribution for all galaxies of the group; *ii*) the contribution to the light of the different components in the BGG; *iii*) the intra-group light. Taking advantage of the deep imaging from VEGAS, the main science goal of this analysis, is to address the mass assembly history of the IC 1459 group (see Sec. 5).

4.1. The low surface brightness features in IC 1459 groups

In Fig. 2 we show an enlarged region of the VST mosaic around IC 1459 in the *g*-band surface brightness levels⁴. This is the region of the group where the majority of the faint low surface brightness features are detected. All of them are in the outskirts of the brightest group member IC 1459. The galaxy shows an extended (≈ 8 arcmin) envelope, down to $\mu_g \sim 27$ mag/arcsec², which appear twisted with respect to the central brightest region of the galaxy and very irregular in shape. It is more elongated in the NE-SW direction, where we detected faint ($\mu_g \sim 26.5$ mag/arcsec²) concentric shells at distance of $\approx 5 - 8$ arcmin from the galaxy centre. In the same range of radii, on the NW, the envelope has prominent sharp edges at the surface brightness levels of $\mu_g \sim 24.5 - 26.5$ mag/arcsec². An elongated thick structure, of ≈ 10 arcmin with $\mu_g \sim 26.5$ mag/arcsec², extends from east to west in the south region of the galaxy. Following Mancillas et al. (2019), this resembles a tidal tail.

The small group member IC 5264 (see Fig. 1) in the SW region turns to be completely embedded in the IC 1459's envelope. We detected an "S-shape" of the disk in IC 1459 with a

thick arc-like tail protruding on the West side (see Fig. 2), of about 3 arcmin and with $\mu_g \sim 26.5$ mag/arcsec².

A detailed inspection of the whole VST mosaic does not show any other low surface brightness feature (at the imaging depth of the observations) in the intra-group space. The colour composite images for the other group members, given in Appendix B, show that all galaxies, except the faintest S0 IC 5269, have an asymmetric outskirts. In particular, the spiral galaxy ESO 406-27 show a prominent plume emerging from the disk in the NE, at which is associated an over-density of the HI gas (see Fig. B.5). All group members are described in Appendix A.

4.2. Isophotal Analysis

In order to map the light and colour distribution for all group members, we have performed the isophotal analysis by using the IRAF task ELLIPSE (the position angle and the ellipticity are free parameters) on the final stacked image in each band, out to the limiting radius estimated for each object (see Sec. 3). The method is the same adopted in the previous studies based on the VEGAS data (Capaccioli et al. 2015; Iodice et al. 2016, 2017b; Spavone et al. 2017b, 2018; Cattapan et al. 2019; Iodice et al. 2019). The isophote fit was performed for each galaxy by masking all the bright sources in the field (stars and background galaxies). In the case of IC 5264 and IC 5269B, which are close/embedded in the diffuse stellar envelope of IC 1459 (see Fig. 2), the isophote fit was performed after subtracting the two-dimensional model⁵ of IC 1459.

From the isophotal analysis, we have derived the azimuthally-averaged surface-brightness, ellipticity (ϵ), and position angle (PA) radial profiles in the *g* and *r* bands, the averaged extinction-corrected colour profiles, and the averaged *g* – *r*, *r* – *i*, and *g* – *i* colour values. In addition, from the growth curve we have estimated the total magnitude and effective radii in each band. Finally, using stellar population synthesis models (Ricciardelli et al. 2012; Vazdekis et al. 2012) with $\log Z/Z_\odot = 0$ and a Kroupa initial mass function and considering the average colour, we have estimated the total stellar mass by using the M/L ratio in the *g* band (Iodice et al. 2017b; Spavone et al. 2018; Cattapan et al. 2019). Results are reported in Table 3 and Table 4. For the BGG, IC 1459, the azimuthally-averaged surface-brightness, ellipticity, and position angle radial profiles are shown in Figure 3. Figure 4 shows the azimuthally averaged extinction-corrected colour profile and the two-dimensional *g* – *r* colour map centred on IC 1459. The surface brightness profiles are PSF-deconvolved (see Capaccioli et al. 2015; Spavone et al. 2017b). For the other group galaxies the color-composite image, the azimuthally-averaged surface-brightness radial profiles in *g*, *r*, and *i* band, and azimuthally-averaged extinction-corrected colour profiles are shown in Appendix B.

4.3. Fitting of the Light Distribution

In order to identify the main components dominating the galaxy light in IC 1459, we have fitted the deconvolved surface-brightness radial profiles in the *g* band. Since our aim is to compare the results of this fit with previously published ones, for consistency we use the *g* band profile, as done for NGC 5018 (Spavone et al. 2018) and NGC 1533 (Cattapan et al. 2019).

The main outcome of the fitting is to map the stellar distribution in the outer envelopes of our sample galaxies. To this

⁴ In this image we modelled and subtracted only the brightest regions of the close foreground stars. This prevent the subtraction of any physical faint feature overlapping the halo of the stars.

⁵ The two-dimensional model of IC 1459 is based on the isophote fit and it was derived by using the task BMODEL in IRAF.

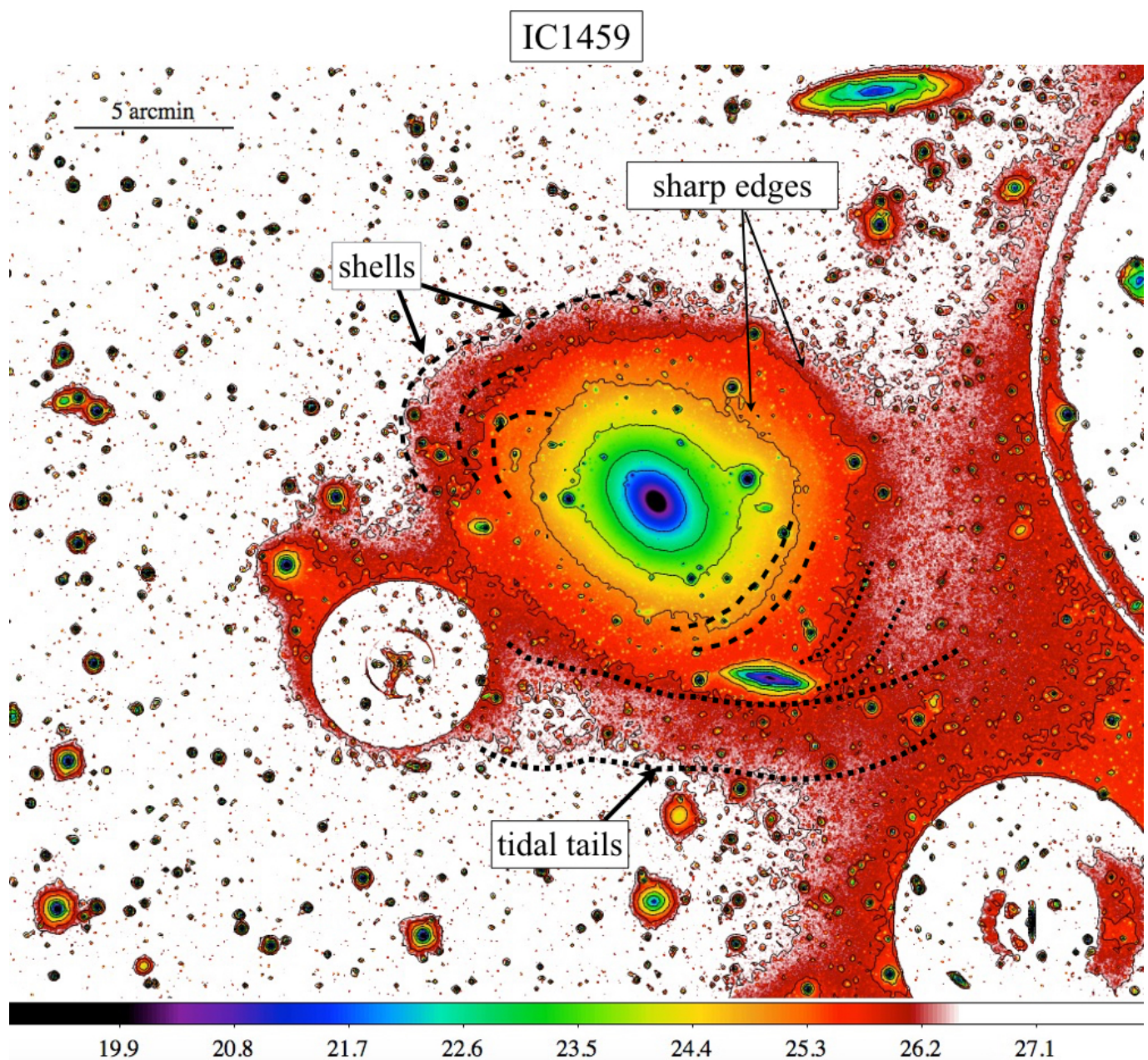


Fig. 2. Enlarged region ($\sim 52' \times 43'$) of the VST mosaic around IC 1459 in the g band. The image is in surface brightness levels, given in the horizontal colour-bar. The solid contours correspond to the following surface brightness levels: 22, 23, 24, 25, 26.4 mag/arcsec². The main low surface brightness features detected in the galaxy outskirts are marked on the image: dotted lines and dashed lines delimit the tidal tails and shells, respectively. The prominent sharp edges on the West side are also indicated with arrows (see text for details).

aim, according to Spavone et al. (2017b), we do not use the χ^2 statistics in our fitting procedure. The data points corresponding to the central regions of the galaxies, in fact, with their small uncertainties have considerable weight in determining the best-fit solution obtained by minimising the χ^2 , while the outer regions with bigger errors have no weight. To avoid this problem, we adopt the same approach described by Seigar et al. (2007); Spavone et al. (2017b) and performed least-square fits using a Levenberg–Marquardt algorithm, in which the function to be minimised is the rms scatter, defined as $\Delta = \sqrt{\frac{\sum_{i=1}^m \delta_i^2}{m}}$, where m is the number of data points and δ_i is the i th residual. In order to

account for fainter stellar envelope in the most luminous ETGs, there is remarkable evidence from the recent deep surveys that the light profiles of these galaxies are not well fitted by a single Sérsic law and at least one additional component is needed to map the outer envelope contribution in the light distribution of the galaxy (see e.g. Seigar et al. 2007; Donzelli et al. 2011; Arnaboldi et al. 2012; Huang et al. 2013; Iodice et al. 2016; Spavone et al. 2017a, 2018).

For this reason we have fitted the azimuthally-averaged surface-brightness radial profiles of IC 1459 combining a Sérsic law and an exponential function. From the total magnitude of

Table 3. Total magnitude and effective radius for the galaxies of the IC 1459 group.

Galaxy	m_g (mag)	$R_{e,g}$ (arcsec)	m_r (mag)	$R_{e,r}$ (arcsec)	m_i (mag)	$R_{e,i}$ (arcsec)
(1)	(2)	(3)	(4)	(5)	(6)	(7)
IC 1459	9.28 ± 0.07	177.00 ± 0.01	8.71 ± 0.07	133.60 ± 0.81	8.49 ± 0.01	50.8 ± 0.19
IC 5269	12.58 ± 0.02	20.91 ± 0.20	12.01 ± 0.02	18.59 ± 0.33	11.24 ± 0.01	18.59 ± 0.33
IC 5269B	12.69 ± 0.02	67.42 ± 0.81	12.27 ± 0.02	68.49 ± 0.89	11.38 ± 0.03	88.31 ± 1.23
IC 5270	12.24 ± 0.03	47.15 ± 1.81	11.72 ± 0.03	49.06 ± 0.89	11.04 ± 0.05	44.16 ± 0.79
IC 5264	12.67 ± 0.03	30.21 ± 0.44	11.89 ± 0.04	34.34 ± 0.76	11.16 ± 0.04	31.55 ± 0.75
ESO 406-27	12.86 ± 0.06	82.58 ± 3.18	12.73 ± 0.09	75.08 ± 5.95	12.38 ± 0.07	49.08 ± 1.09
NGC 7418	10.31 ± 0.03	161.00 ± 2.49	10.01 ± 0.03	143.90 ± 2.36	9.94 ± 0.01	57.48 ± 0.37
NGC 7421	11.93 ± 0.01	39.87 ± 1.83	11.53 ± 0.01	32.27 ± 0.07	10.81 ± 0.01	31.49 ± 0.16
IC 5273	10.70 ± 0.04	99.77 ± 2.01	10.52 ± 0.03	77.70 ± 1.30	10.23 ± 0.02	41.11 ± 0.38

Notes. Col. 1 - Galaxy name. Col. 2 and Col. 3 - total magnitude and effective radius in g band. Col. 4 and Col. 5 - total magnitude and effective radius in r band. Col. 6 and Col. 7 - total magnitude and effective radius in i band.

Table 4. Colours, and total stellar mass for the galaxies of the IC 1459 group.

Galaxy	$A_{g'}$ (mag)	$A_{r'}$ (mag)	$A_{i'}$ (mag)	$g-r$ (mag)	$r-i$ (mag)	$g-i$ (mag)	$(M/L)_g$ (M_\odot/L_\odot)	$L_{\text{tot},g}$ ($\times 10^{10} L_\odot$)	M_{tot}^* ($\times 10^{10} M_\odot$)
(1)	(2)	(3)	(4)	(5)	(6)	(7)	(8)	(9)	(10)
IC 1459	0.060	0.044	0.033	0.84 ± 0.31	0.51 ± 0.20	1.36 ± 0.30	5.695	17.70	100.80
IC 5269B	0.060	0.044	0.033	0.49 ± 0.10	0.65 ± 0.09	1.14 ± 0.18	0.656	0.77	0.50
IC 5269	0.062	0.045	0.034	0.77 ± 0.25	0.71 ± 0.06	1.47 ± 0.19	3.921	0.85	3.32
IC 5270	0.052	0.038	0.029	0.72 ± 0.09	0.65 ± 0.12	1.38 ± 0.15	2.335	1.16	2.71
IC 5264	0.077	0.056	0.042	0.79 ± 0.06	0.81 ± 0.02	1.60 ± 0.05	4.301	0.78	3.35
ESO 406-27	0.081	0.059	0.044	0.34 ± 0.20	0.45 ± 0.16	0.79 ± 0.16	0.488	0.65	0.32
NGC 7418	0.060	0.044	0.033	0.66 ± 0.29	0.44 ± 0.57	1.09 ± 0.74	1.585	6.86	10.87
NGC 7421	0.056	0.041	0.031	0.66 ± 0.24	0.68 ± 0.06	1.35 ± 0.23	1.585	1.54	2.44
IC 5273	0.047	0.034	0.026	0.54 ± 0.15	0.51 ± 0.28	1.05 ± 0.40	0.701	4.78	3.36

Notes. Col. 1 - Galaxy name. Col. 2, Col. 3 and Col. 4 - extinction correction in the g , r , and i band from NED. Col. 5, Col. 6 and Col. 7 - averaged extinction-corrected $g-r$, $r-i$, and $g-i$ colour value. Col. 8 - mass-to-light ratio in g band. Col. 9 - total stellar luminosity in g band. Col. 10 - total stellar mass.

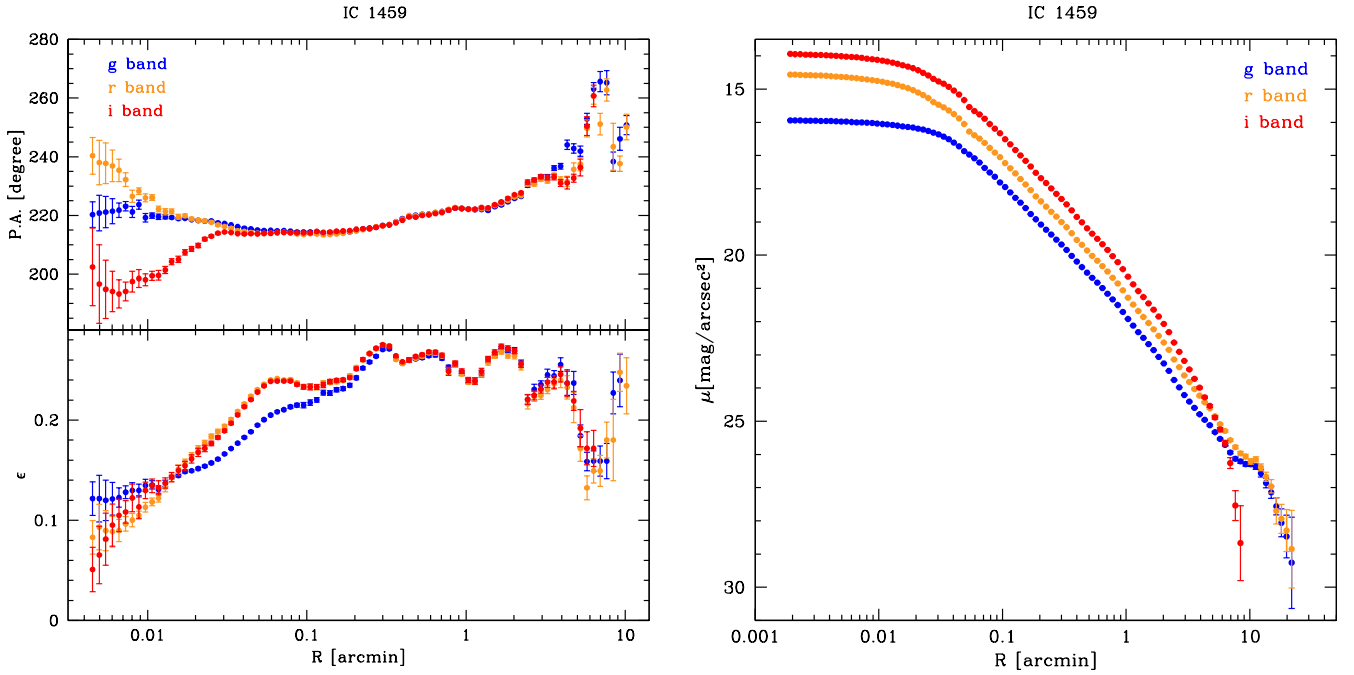


Fig. 3. Results from the isophotal analysis for IC 1459. Ellipticity and position angle radial profiles are shown in the left lower and top panels, respectively. The azimuthally-averaged and PSF-deconvolved surface-brightness radial profile of IC 1459 are plotted in the right panel.

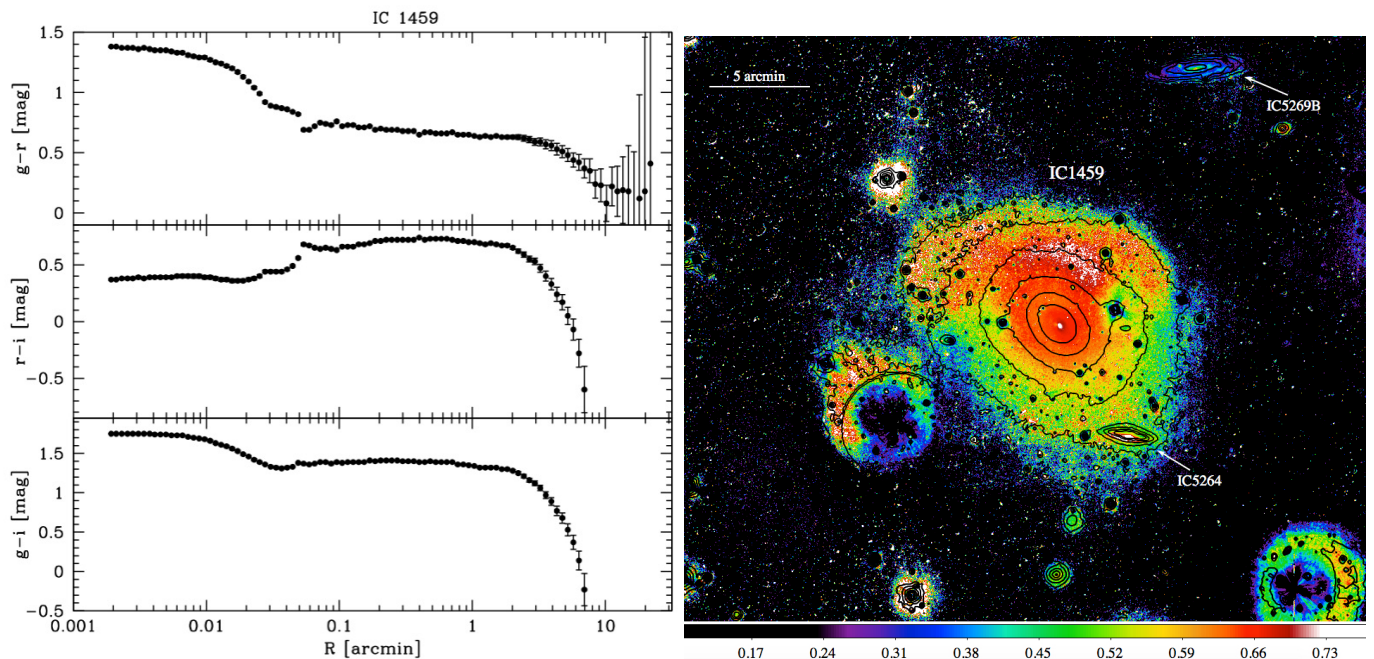


Fig. 4. Left panel: azimuthally-averaged, PSF-deconvolved, and extinction-corrected colour radial profiles of IC 1459. Right panel: two-dimensional colour map centred on IC 1459, the image size is $35.42:7 \times 29.05:7$ with north at the top and east on the left. The horizontal colour bar gives the $g - r$ colour scale. The solid contours correspond to the following surface brightness levels in the g band: 22, 23, 24, 25, 26.4 mag/arcsec².

the Sérsic and exponential component, $m_{\text{tot},1}$ and $m_{\text{tot},2}$ respectively, taking into account the stellar mass-to-light ratio derived from the average $g - r$ colours (see Tab. 4), we derived the relative contribution of the outer envelope with respect to the total stellar mass of the galaxy (it is f_h in Table 5) which is about the 37%. Results are listed in Table 5 and shown in Figure 5.

Numerical simulations by Cooper et al. (2013, 2015); Pillepich et al. (2018) suggest that the surface brightness profile of BCGs/BGGs could be described by the superimposition of three components. In these simulations, the first Sérsic law represents the central *in-situ* component; the second Sérsic law and the third exponential function represent the accreted component, the relaxed and un-relaxed respectively. As discussed in detail by Spavone et al. (2017a,b), in order to compare observations and theoretical predictions, we used numerical simulations as “prior” guide for the decomposition, and fitted the light distribution of IC 1459 also with a three-component model, where the inner Sérsic component should “mimic” the *in-situ* component predicted by the above numerical simulations. The fitted parameters are listed in Table 5. Figure 5 shows the results of the three-component fits. Looking at the rms scatter Δ of the fit, we can clearly see that by adding the third component we achieve an improvement of at least 4%. Since the expected value of Δ scales as $\sqrt{(m - k)/m}$ (see Seigar et al. (2007)), where m is the number of measured points (~ 70 in our case) and k is the number of free parameters, we would need 11 free parameters to obtain an improvement of 4%. This means that the improvement we obtain in our fit is not only due to the introduction of additional free parameters, as already shown by Seigar et al. (2007) and Spavone et al. (2017b).

From the three-component model, we have estimated the transition radius $R_{\text{tr}} = 3:1 \approx 25.7$ kpc, which is the distance from the galaxy centre at which the unrelaxed component starts to dominate the light distribution of the BGG (Cooper et al. 2013). From the two accreted stellar components, the relaxed

and un-relaxed ones, described by the second Sérsic law and exponential function, we estimate the total accreted mass fraction of 87% in IC 1459, which corresponds to $8.77 \times 10^{11} M_{\odot}$ (see Table 6). This is the relative contribution of the accreted components with respect to the total stellar mass of the galaxy, $f_{h,T}$, to be compared with the predictions for this quantity by the numerical simulations cited above. The comparison is given in Fig. 7 and commented in Sec. 6.1. The error bars on the datapoint have been derived by means of error propagation on M_{\star} and M_{acc} , which are 0.02 and 0.04, respectively. Table 6 reports the values of transition radius, mass-to-light ratio, total stellar mass, and accreted mass fraction of IC 1459.

4.4. Intragroup Light

As stated before, from a detailed inspection of the deep VST mosaic we do not detect any intragroup low surface brightness features in the form of stellar tails or streams between and/or around the group members, except for those in the outskirts of IC 1459 (see Sec.4.1 and Fig. 2). Therefore, we consider this area as the bulk of IGL and focused on it to estimate the total flux in this component. To this aim, we have modelled the light distribution in the g band of the dominant member IC 1459 with the IRAF task BMODEL. This task creates a two-dimensional noiseless photometric model of the galaxy from the result of the isophotal analysis generated by ELLIPSE, by taking into account the variations in the ellipticity and position angle. We have derived the residual image by subtracting the two-dimensional model from the parent image. All the foreground and background sources in the residual image were masked. In particular, for the three brightest stars HD 216666 in the area ($\alpha_{J2000} = 22^{\text{h}}55^{\text{m}}14^{\text{s}}.947$ and $\delta_{J2000} = -36^{\circ}23'19''.18$), HD 216781 ($\alpha_{J2000} = 22^{\text{h}}56^{\text{m}}12^{\text{s}}.13$ and $\delta_{J2000} = -36^{\circ}40'49''.3$), and HD 216972 ($\alpha_{J2000} = 22^{\text{h}}57^{\text{m}}50^{\text{s}}.33$

Table 5. Best fitting structural parameters for the multi-component fit of the surface-brightness radial profile of IC 1459 in the g band.

Models	$R_{e,1}$		n_1	$\mu_{e,1}$	$R_{e,2}$		n_2	$\mu_{e,2}$	r_h		μ_0	$f_{h,T}$
	(arcsec)	(kpc)		(mag arcsec $^{-2}$)	(arcsec)	(kpc)		(mag arcsec $^{-2}$)	(arcsec)	(kpc)	(mag arcsec $^{-2}$)	
(1)	(2)	(3)	(4)	(5)	(6)	(7)	(8)	(9)	(10)			
2	53.79 ± 0.06	7.15	5.3 ± 0.7	21.7 ± 0.5	390 ± 1	52.61	25.18 ± 0.01	37%
3	5.54 ± 0.12	0.67	1.61 ± 0.06	18.19 ± 0.04	54 ± 1	7.28	2.12 ± 0.12	21.69 ± 0.05	329 ± 4	44.38	24.49 ± 0.11	87%

Notes. Best fit parameters of the PSF-deconvolved light profiles decomposition: *Col. 1* - number of functions of the multi-component fit applied. *Col. 2*, *Col. 3*, and *Col. 4* - effective radius, Sérsic index, and effective surface brightness of the first Sérsic component. *Col. 5*, *Col. 6*, and *Col. 7* - effective radius, Sérsic index, and effective surface brightness of the second Sérsic component. *Col. 8*, and *Col. 9* - scale radius, and central surface brightness of the exponential component. *Col. 10* - accreted mass fraction.

and $\delta_{J2000} = -36^\circ 32' 45'' 8$ ⁶, masks extend out to regions where scattered light is detected (see Fig. 2). The IGL region is defined with the IRAF task POLYMARK and it is about 23 arcmin² around IC 1459. From the fit of the light profiles, we know that the stellar envelope starts to dominate at $R \geq R_{tr} = 3.1 = 25.77$ kpc (see Sec. 4.3). Therefore, for the IGL estimate we account for the flux from $R \geq R_{tr}$, and the inner regions of the galaxy (at smaller radii) are masked.

From the defined regions, we have derived the integrated extinction-corrected magnitude of the IGL. The total luminosity of the IGL in g band is $5.25 \times 10^9 L_\odot$, that accounts for the 2% of the total light of the group and 3% of the light of IC 1459 (see Table 7). The error estimate on the flux in the selected area takes into account all sources that contributed to the residual fluctuations in the sky background, as given in Sec. 3.

5. A deep view of the IC 1459 Group

Deep OmegaCAM@VST data allow us to map the azimuthally-averaged surface brightness of IC 1459 down to $\mu_g = 29 \pm 1$ mag arcsec $^{-2}$ and $\mu_r = 29 \pm 1$ mag arcsec $^{-2}$ at $R = 21.83 \approx 181.1$ kpc ($\sim 7.4R_e$ in g and $\sim 9.8R_e$ in r band) (see right panel of Figure 3). Images in the i band are shallower (see Tab. 2 and Sec. 3), which cause the observed drop of the surface brightness profile in this band (see Fig. 3). IC 1459 is the biggest and the reddest galaxy of the group, with $R_{e,g} \approx 23.9$ kpc and $g - r = 0.84$ mag (Table 3). By fitting the light distribution we found that the outer stellar envelope starts to dominates the light for $R \geq 5$ arcmin (see Sec. 4.3 and Tab. 5). The other group members are LTGs, except for IC 5269 that is classified as an S0 (see Fig. 1). Main properties of LTGs (i.e. total luminosity, effective radii and average colours) are given in Table 3 and Table 4.

The enlarged region of the VST mosaic around IC 1459 in the g -band surface brightness levels (see Fig. 2) highlights the structure of the IC 1459 outer envelope (i.e. at $R \geq 5$ arcmin). There are shells in the North-East and South-West regions and prominent sharp edges on the west side. We detected an elongated tidal tail on the south, and thick arc-like tail protruding on the West side of the small group member IC 5264. The isophotal analysis shows that the outer envelope has a twist in the position angle profile of about 40 degrees and a scatter in the ellipticity profile being roundish (see left panel of Figure 3).

From the averaged colour profile (Figure 4, left panel), inside 1 arcmin (~ 8 kpc) IC 1459 has redder colours, where $g - r$ varies in the range 0.5–1.5 mag. This is the region where Forbes et al. (1995, and references therein) detected an arcsec-scale dust lane crossing the galaxy nucleus. At larger radii, the colour profiles decline toward bluer colours, with $g - r \leq 0.5$ mag. The two-dimensional colour map (Figure 4, right panel) shows an

asymmetric distribution of the colour: in the north, there is a arc-like structure, extending from East to West, characterised by very red colours ($g - r \geq 0.6$ mag). This structure corresponds to the region where shells are detected in the envelope. In the region of the tidal tail (in the south) the envelope has bluer colours ($g - r \approx 0.6$ mag). The small peculiar LTG ESO 406-27 in the group, which is located in this region, is the bluest galaxy of the group ($g - r \sim 0.34$, Table 4). The existence of the blue tidal tails close to ESO 406-27 might confirm the previous hypothesis that there is a possible ongoing interaction of this galaxy with IC 1459 (Serra et al. 2015; Saponara et al. 2018).

Figure 1 shows the VST g band mosaic of the group with the HI map from Oosterloo et al. (2018). There is a lot of HI associated to LTGs, showing a different degree of asymmetry and off-centre distribution respect to the stellar disk. In the region of the BGG there are signatures of HI stripping from gas-rich galaxies (Saponara et al. 2018), like the north-east to south-west low surface-brightness HI tail (Oosterloo et al. 2018). The possible HI donors of these debris are IC 5264 and ESO 406-27 (Saponara et al. 2018; Oosterloo et al. 2018). In the NE of IC 1459, the HI seems not associated with galaxies: the deep VST images shows that this is the region where shells in the envelope are detected. In the southern part of the IC 1459 envelope, the HI distribution is also elongated EW, overlapping the region where the faint tidal tail is found (see Fig. 2). Furthermore, more in the south, we found a faint diffuse light over-density north to ESO 406-27 (see Fig. B.5), which would be consistent with the interaction scenario proposed by Serra et al. (2015), Saponara et al. (2018) and Oosterloo et al. (2018) which involves IC 5264 and ESO 406-27.

In conclusion, the faint features detected in the IC 1459's envelope provide evidence of the on-going accretion process on the BGG. Furthermore, the interaction and tidal effects could be responsible of HI stripped debris and of the faint optical counterparts found in two group members (Kilborn et al. 2009; Serra et al. 2015; Saponara et al. 2018).

6. IC 1459 versus other Loose Groups of Galaxies

In this section we compare the main observed properties of the IC 1459 group with those available for the other two groups of galaxies centred on NGC 5018 (Spavone et al. 2018) and NGC 1533 (Cattapan et al. 2019). The comparison is motivated by consistency in the data set and in the total mass of the systems. All groups are targets of the VEGAS sample. Therefore, all data were obtained with the same telescope and with the same observing strategy, so they have comparable depth and accuracy. Furthermore, for the data analysis (i.e. isophote fit, fitting of the surface brightness profiles, colour estimate) we adopted the same tools and procedures described in Sec. 4. In addition, the three groups have the virial mass of the same order of magnitude. NGC 5018 and NGC 1533 groups have comparable virial

⁶ The stars coordinates are from HYPERLEDA

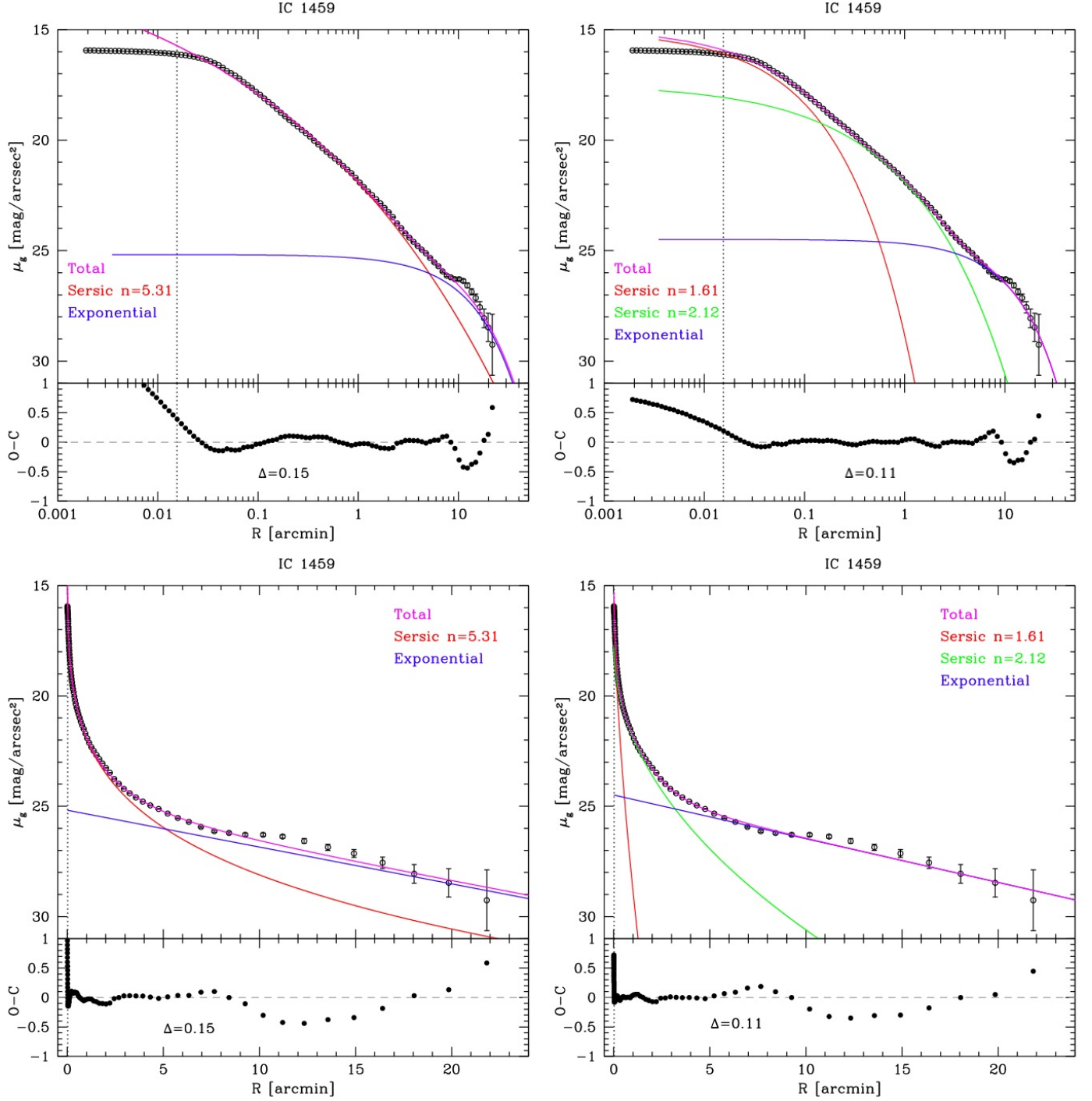


Fig. 5. *g* band surface-brightness radial profile of IC 1459 (black open circles) on a logarithmic (top panels) and linear scale (bottom panels) fitted with a two-component model (left panels) and with a three-component model (right panels). The red solid line is the first Sérsic component, the green solid line is the second Sérsic component, the blue solid line is the exponential component, and the magenta solid line marks the model of the total light distribution. The black vertical dotted line marks the core of the galaxy which was excluded in the fit ($R < 0''.9$). The $O - C$ panel (black filled circles) represents the residual between the azimuthally-averaged surface-brightness radial profile and the multi-component model. Δ is the rms scatter minimised by the Levenberg-Marquardt algorithm (Seigar et al. 2007).

radius and mass, with $R_{\text{vir}} = 0.4$ Mpc and $M_{\text{vir}} \sim 7 \times 10^{12} M_{\odot}$ for NGC 5018, and $R_{\text{vir}} = 0.4$ Mpc and $M_{\text{vir}} \sim 5 \times 10^{12} M_{\odot}$ for NGC 1533 (Gourgoulhon et al. 1992; Firth et al. 2006), whereas IC 1459 is a massive system, with $R_{\text{vir}} = 0.21$ Mpc and $M_{\text{vir}} \sim 3.710^{13} M_{\odot}$ (see Sec. 2 and Brough et al. 2006).

In the following sections, we compare the characteristics of the BGGs, the stellar halo properties, the amount of IGL, and

the HI mass and distribution. This helps to trace the different evolutionary stages and how this could reflect in the observed properties.

An overall and preliminary picture of the evolutionary stage of the groups is carried out here using the color-magnitude diagram (CMD). Here it is possible to trace the galaxy transformation from active and star-forming (Blue Cloud, BC) to passively

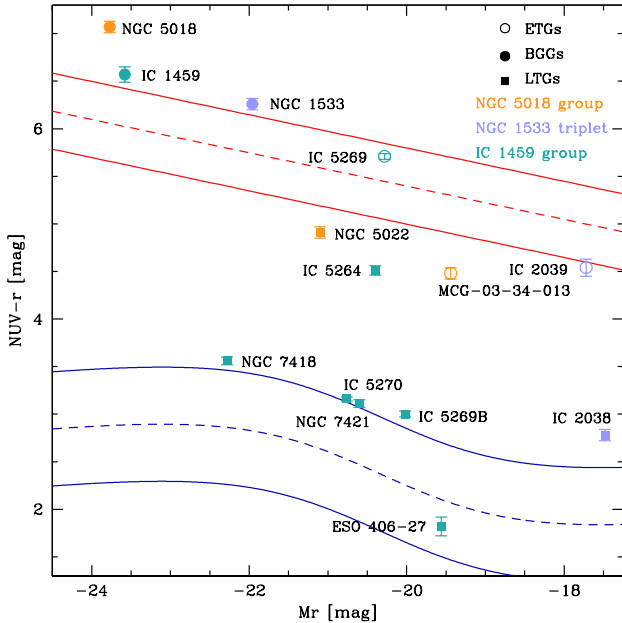


Fig. 6. M_r vs. $(NUV - r)$ colour–magnitude diagram of the three loose groups: the NGC 5018 group (orange points), the NGC 1533 triplet (mauve points), and the IC 1459 group (teal points). The Wyder et al. (2007) fits (dashed lines), plus the error estimations (solid lines), to the Red Sequence (red lines) and Blue Cloud (blue lines) are shown. Open circles mark early-type galaxies (ETGs), filled circles mark the brightest group galaxies (BGGs), and filled squares mark late-type galaxies (LTGs). The NUV data are from NED, while the r band data for the NGC 5018 group are from Spavone et al. (2018), for the NGC 1533 triplet are from Cattapan et al. (2019), and for the IC 1459 group are presented in this work.

(Red Sequence, RS) evolving system via the Green Valley (GV, see e.g. Mazzei et al. 2014, and references therein). Figure 6 shows the CMD of the three analysed low density environments. The BGG of the NGC 5018 group, NGC 5018, seems to be a typical red and dead ETG, and the other two galaxies (NGC 5022 and MCG-03-34-013) are in the GV approaching the RS. The very red NUV- r colours for NGC 5018 could be reasonably due to the large amount of dust in the galaxy centre (Spavone et al. 2018), which affects the NUV flux. In the NGC 1533 triplet the BGG, NGC 1533 is in the RS, while the other ETG (IC 2039) is very close to the RS, and the LTG (IC 2038) has just left the BC. The CMD of the entire backbone of the Dorado group, including the NGC 1533 triplet, has been shown by Cattapan et al. (2019). The Dorado backbone has an extended and rich RS. IC 1459 and IC 5269 are the two ETGs of the IC 1459 group and they lie in the RS, as expected. IC 5264 is the LTG that lies in projection of the stellar halo of IC 1459 and it is in the GV. All the other LTGs, except for ESO 406-27 which is in the BC, are leaving the BC to migrate in the GV.

This means that the IC 1459 group is a typical young galaxy group with a significant BC and a depopulated RS. And on the other hand the NGC 5018 group represents what happens for more evolved galaxy systems which have a well defined RS and a poor or empty BC (Cattapan et al. 2019, and references therein).

6.1. The accreted mass fraction of BGGs

The three BGGs we analyse are NGC 5018, NGC 1533 and IC 1459. IC 1459 is the brightest ($L_{\text{tot}}^* = 1.77 \times 10^{11} L_{\odot}$), more massive ($M_{\text{tot}}^* = 10.08 \times 10^{11} M_{\odot}$) and reddest galaxy ($g - r = 0.84$ mag). While NGC 1533 is the less luminous ($L_{\text{tot}}^* = 2.99 \times 10^{10} L_{\odot}$) and less massive galaxy ($M_{\text{tot}}^* = 2.9 \times 10^{11} M_{\odot}$). NGC 5018 is the bluest galaxy ($g - r = 0.7$ mag). The properties of the BGGs are listed in Table 6. In Figure 7 we show the accreted mass fraction as a function of the total stellar mass for the analysed BGGs/BCGs in VEGAS (Iodice et al. 2016, 2017a; Spavone et al. 2017b, 2018; Cattapan et al. 2019) and for the other BGGs/BCGs in the literature (Seigar et al. 2007; Bender et al. 2015). We compare these results with the theoretical predictions of cosmological galaxy formation by Cooper et al. (2013, 2015) and with the Illustris simulations by Pillepich et al. (2018, their Figure 12). We find that the accreted mass fraction for the three BGGs (IC 1459, NGC 5018 and NGC 1533) is in the range of 78% – 92% (Table 6). These values are comparable with those obtained for other BCGs and BGGs in VEGAS sample, as well as with literature data (see Fig. 7). Moreover, the accreted mass fraction estimated for IC 1459 and previously for NGC 5018 and NGC 1533 is consistent with the theoretical predictions, which suggest that stars accreted by BCGs/BGGs in the stellar mass range $10^{11} - 10^{13}$ account for most of their total stellar mass (Cooper et al. 2013; Pillepich et al. 2018).

The above result also suggests that the accreted stellar mass fraction seems to be a function of the total stellar mass rather than of the environment, since the BGGs have comparable accreted mass to the bright cluster members (Figure 7). This lack of correlation between accreted mass fraction and environment is a very recent studied topic and it is developed for BCGs by DeMaio et al. (2018).

6.2. The stellar envelope of the BGGs

By fitting the light distribution, we were able to set the scales of the different components in the galaxy structure. In particular, we estimated the transition radius where the outer stellar and faint envelope starts to dominate the light (see Sec. 4.3). The stellar envelopes of the three BGGs studied in this work occur at surface brightness levels $25.1 < \mu_g < 27.2$ mag arcsec $^{-2}$ (see Table 6), which is comparable with the surface brightness of the stellar envelopes observed in other BCGs (Spavone et al. 2017a, $24.0 < \mu_g < 27.8$ mag arcsec $^{-2}$) and even consistent with the theoretical predictions. In the three BGGs, the transition in the surface brightness profiles also corresponds to a transition in the ellipticity, position angle and colour profiles. In particular, the outer isophotes are more elongated or rounder than the inner ones and are twisted (see Fig. 3 and Spavone et al. 2017a, 2018; Cattapan et al. 2019).

In Figure 8 we have compared the azimuthally-averaged surface brightness (in the g band) and colour profiles for the three BGGs, scaled to their effective magnitude, as a function of R/R_e . This reveals that NGC 5018 has the most extended envelope, out to $30 R_e$, which is also quite red ($(g - r)_{R > R_{tr}} = 0.94$ mag). IC 1459 and NGC 1533 have smaller ($\sim 10 R_e$) and bluer envelopes, with $(g - r)_{R > R_{tr}} = 0.44$ mag and $(g - r)_{R > R_{tr}} = 0.49$ mag, respectively. At radii larger than R_{tr} (i.e. $\geq 2 R_e$), the surface brightness profiles show that the contribution to the total light from the stellar envelope in NGC 5018 and IC 1459 is larger than that in NGC 1533. This is consistent with an higher accreted mass fraction estimated in the former two galaxies (see Tab. 6).

Table 6. Main properties of the BGGs sample.

BGG	$g-r$ (mag)	$(M/L)_g$	M_{tot}^* ($\times 10^{11} M_{\odot}$)	$f_{h,T}$	$M_{\text{tot acc}}^*$ ($\times 10^{11} M_{\odot}$)	R_e (kpc)	R_{tr}/R_e	μ_{tr} (mag arcsec $^{-2}$)	$(g-r)_{R<R_{tr}}$ (mag)	$(g-r)_{R>R_{tr}}$ (mag)
(1)	(2)	(3)	(4)	(5)	(6)	(7)	(8)	(9)	(10)	(11)
NGC 5018	0.70 ± 0.20	1.97	2.9	92%	2.7	6.37	5.37	26.6	0.78	0.94
NGC 1533	0.77 ± 0.05	3.92	1.17	78%	0.91	6.35	2.80	27.2	0.77 ± 0.04	0.49 ± 0.29
IC 1459	0.84 ± 0.31	5.70	10.08	87%	8.77	24.47	1.05	25.1	0.89 ± 0.29	0.44 ± 0.11

Notes. Col. 1 - BGGs name. Col. 2 - averaged extinction-corrected $g-r$ colour value. Col. 3 - mass-to-light ratio in g band. Col. 4 - total stellar mass. Col. 5 and Col. 6 - total accreted stellar mass fraction from the multi-component fit in g band and value in solar masses. Col. 7 - Effective radius in g band. Col. 8 and Col. 9 - transition radius normalised to the effective radius and corresponding surface brightness. Col. 10 and Col. 11 - averaged extinction-corrected $g-r$ colour value inside and outside the transition radius.

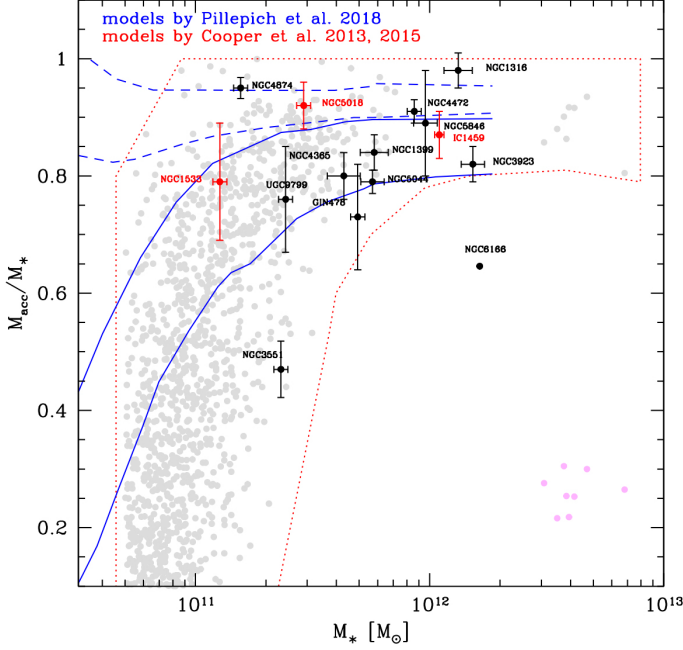


Fig. 7. Accreted mass fraction as a function of total stellar mass for ETGs. The measurements for NGC 5018, NGC 1533, and IC 1459 (from the three-components fit) are given as red circles. Black circles correspond to other BGGs/BCGs from the literature (Seigar et al. 2007; Bender et al. 2015; Iodice et al. 2016, 2017a; Spavone et al. 2017b, 2018). The region within the red dashed lines and the grey filled circles correspond to the predictions of cosmological galaxy formation simulations by Cooper et al. (2013, 2015). The regions brackets by the blue continuous and dashed lines indicate the accreted mass fraction measured in the Illustris simulations by Pillepich et al. (2018, ; see their Figure 12) within 30 kpc and outside 100 kpc, respectively. Magenta filled circles show the mass fraction associated with the streams from table 1 in Cooper et al. (2015).

According to the theoretical predictions on the mass assembly on the BCGs and BGGs, the morphology of the outskirts, the shape of the light profiles and colour distribution reflect the different accretion processes and progenitors (Cooper et al. 2010; D’Souza et al. 2014; Monachesi et al. 2019; Mancillas et al. 2019). The gradual accretion of small-mass satellites produces streams, the intermediate and major merging generates shells and tidal tails. In the outskirts of three BGGs, the deep VEGAS images have shown such kind of features, suggesting that the mass assembly is still ongoing. The most prominent and luminous tidal tails are observed in the NGC 5018 group, in the intra-group space and protruding from the BGG (Spavone et al. 2018). In IC 1459 (this work) and in NGC 1533 we observe very faint tidal tail, which are probably tracing the interaction with

the smaller group members close to the BGG, and several shells in the outskirts (Cattapan et al. 2019).

According to Mancillas et al. (2019), the evolution of the number of tidal tails does not change with the age of the BCG/BGG, the expected number is from 1 to 3 at maximum and have a short survival time of ~ 2 Gyr. Stellar streams show a peak in number (reaching 8 to 10) around 10 Gyr of the galaxy age, decreasing in number for older galaxies, since they tend to be dissolved in the halo. Shells strongly depend on the inclination, therefore the prediction on the detectable number changes from 4 to 8 for a galaxy with an age of 10 Gyr. Both streams and shells are longer-lived than tidal tails, surviving until 4 Gyr. Given that, and taking into account that the last burst of star formation for NGC 5018 is about 4 Gyr (Spavone et al. 2018), whereas in IC 1459 and NGC 1533 it is older (around 10 Gyr) the expected number of tidal tails is consistent with the observations in the same range of surface brightness levels. The number of shells and streams observed in IC 1459 and NGC 1533 is also consistent with simulations in the range of age estimated for these two galaxies. The absence, or few faint, streams and shells in NGC 5018 is also expected from simulations for galaxies of comparable age.

Summarising, the difference or similarity in the global properties (light profiles and substructures) of the stellar envelope in three BGGs might constrain the phase and/or the mechanism in the mass assembly. In particular, NGC 5018 might have experienced strong tidal forces in the latest 2 Gyr during the interaction with the companion bright galaxy, which lead to the prominent tidal tail. Differently, since the IC 1459 and NGC 1533 groups are populated by less luminous galaxies close to the BGG, their stellar halo is assembling by minor and intermediate merging, which shaped the observed shells and streams.

6.3. Intragroup Light

In Figure 9 (top panel) we compare the fraction of IGL with respect to the total light in the group, as function of the virial mass, available for several groups of galaxies, including the estimates we derived for three systems discussed in this work. Although the sample is composed of eight groups in total, the large scatter suggests that there is no clear trend of IGL with the virial mass. For massive cluster of galaxies ($M_{vir} \geq 10^{13}$), this result would be consistent with theoretical predictions from Contini et al. (2014) and Rudick et al. (2011) where the relations between ICL and virial mass is quite flat. On the other hand, the different IGL values found in the three groups is consistent with previous observations indicating that the higher the ETGs/LTGs ratio, the greater the IGL component is (Da Rocha et al. 2008). As pointed out by (Da Rocha et al. 2008), the low IGL fraction is expected for groups that are LTGs dominated and have HI still in the discs

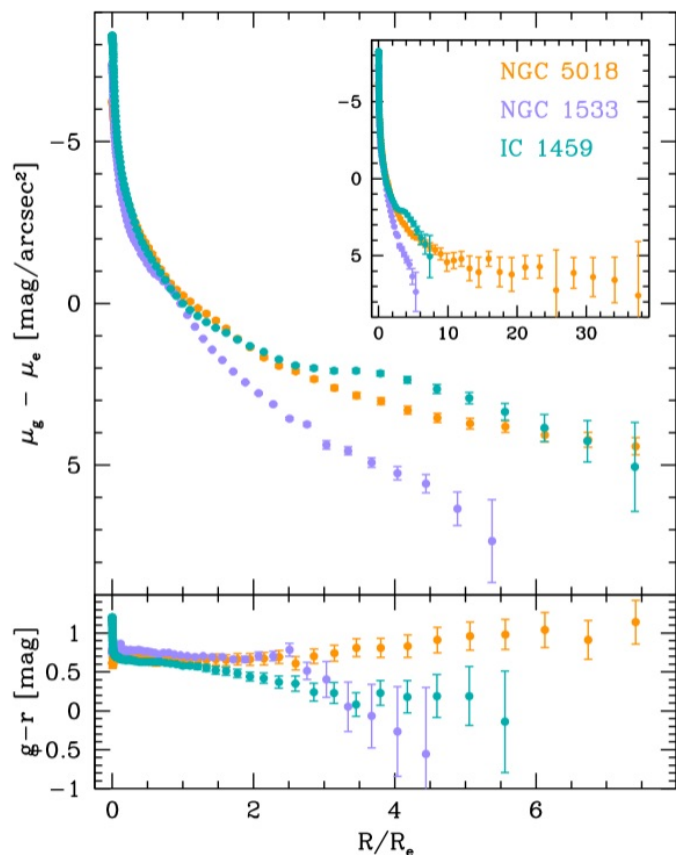


Fig. 8. Azimuthally-averaged surface-brightness (top panel), and colour normalised (bottom panel) radial profiles of NGC 5018 (orange), NGC 1533 (mauve) and IC 1459 (teal) in g band scaled to their effective surface brightness, μ_e , as a function of the semi-major axis normalised to the effective radius, R/R_e .

of the galaxies. The NGC 5018 group and the NGC 1533 triplet are composed of two ETGs and one LTGs (Spavone et al. 2018; Cattapan et al. 2019). While the IC 1459 group counts only two ETGs, IC 1459 and IC 5269, i.e. the ETGs-to-LTGs ratio is quite low, ETGs/LTGs = 0.29 (Table 7). The IGL component of the NGC 5018 group is the highest ($\sim 41\%$) between the three group studied here. A smaller fraction of IGL is derived for the other two systems, it is $\sim 8\%$ for NGC 1533 triplet and $\sim 2\%$ for IC 1459 group (Table 7). Compared to the other two groups, IC 1459 has a large amount of HI associated to the LTGs group members. All others groups of galaxies included in Fig. 9 are Hickson Compact Group (HCG) of galaxies, which are usually characterised by an high ETGs/LTGs ratio (Hickson et al. 1992). The IGL fraction obtained for NGC 5018 (Spavone et al. 2018) is similar to the IGL estimated for HCG 90 (White et al. 2003), which is a strongly interacting system with $L_{\text{IGL}}/L_{\text{Group}} \sim 38\%$ of comparable virial mass. The HCG88 is the only system of the HCG sample that shows no IGL component, down to the surface brightness detection limit (Da Rocha et al. 2008).

The above comparison suggests that, even considering the different detection limit of the observations and the slightly different approach to estimate the intra-group diffuse light, the IGL estimate for the three groups analysed in this work is consistent with previous values for groups of galaxies of comparable virial mass. Values also agree with fractions of ICL quoted in the literature, which ranges from 10 to 40% going from groups

to clusters (e.g. Feldmeier et al. 2004; Zibetti et al. 2005; McGee & Balogh 2010; Toledo et al. 2011).

The fraction of diffuse light in groups and cluster predicted from numerical simulations also spans the same range of values. Predictions from Sommer-Larsen (2006) are $\sim 12\% - 45\%$, while more recently Contini et al. (2014) found $\sim 10\% - 40\%$. The amount of ICL depends on the formation mechanisms. About 5 to 25% of the diffuse light builds up by the infalling galaxies in the potential well of the BCG/BGG during the mass assembly history. Theoretical works predict that the bulk of the ICL is produced by the most massive satellite galaxies, $M \sim 10^{10-11} M_{\odot}$ (Purcell et al. 2007; Contini et al. 2014; Martel et al. 2012). The contribution to the diffuse light from lower-mass galaxies ($M \leq 10^9 M_{\odot}$) is very little, even if they are more numerous. Therefore, the low amount of IGL detected in the IC 1459 group might be connected to the absence in the group of a comparable mass galaxy that is interacting with the BGG (see Tab. 4).

6.4. HI distribution versus diffuse light

In this section, for the three groups studied in this work, we aim at comparing the HI distribution around the group members and in the intra-group space with the location of the LSB features detected. The HI distribution in the NGC 5018 group and in NGC 1533 triplet results from the ongoing tidal interactions between group members, which are stripping the cold gas from the LTGs (Spavone et al. 2018; Cattapan et al. 2019). The debris of tidal stripping are located in the outskirts of the BGGs, i.e. NGC 5018 and NGC 1533, in the form of arc-like structures or extended tails. From the deep VEGAS data, we found the optical counterpart for some of the intra-group HI features, at very faint levels $\mu_g \approx 28 - 30$ mag arcsec⁻².

The IC 1459 group shows a different HI distribution. The HI is mainly associated with the group members and it follows the distribution of galaxies along a thick filament in the North-South direction (Kilborn et al. 2009; Saponara et al. 2018). In addition, Figure 1 shows that there are few HI over-densities that seem not to be associated at any optical feature. The most prominent are close to IC 1459, on the SE and on the NE side. As pointed out in Sec. 4.4, the SE over-density might be associated with the stellar faint tail detected on the south of IC 1459, and linked to the ongoing interaction involving IC 5264 and ESO 406-27 (Saponara et al. 2018; Oosterloo et al. 2018).

A clear difference between the IC 1459 group and the other two groups, NGC 5018 and NGC 1533, also arises by comparing the IGL component with the total HI mass of the group (i.e. galaxies and intragroup HI). The fraction of IGL light decreases as the HI mass increases, see Fig. 9 (lower panel) and Table 7. Figure 9 suggests that this trend, i.e. lower amount of intra-cluster diffuse light is found in groups with higher content of HI gas, seems also confirmed for other groups of galaxies (with available HI and IGL measurements).

To conclude, by correlating the HI distribution and content with the LSB features and IGL amount, the IC 1459 group seems to be in a different evolutionary phase with respect to the NGC 5018 and NGC 1533 groups. The low amount of IGL, the large HI content and its regular distribution might indicate that the IC 1459 group is still assembling. This would be in agreement with Saponara et al. (2018), who suggested that, given the small HI velocity gradient in the south-southeast direction of IC 1459, in combination with the high number of gas-rich members and low velocity dispersion, the group could be in a first stage of evolution.

Table 7. Properties of galaxy group sample.

Group	N	ETGs/LTGs	$m_{\text{IGL},g}$ (mag)	$L_{\text{IGL},g}$ ($\times 10^9 L_\odot$)	$(L_{\text{IGL}}/L_{\text{BGG}})_g$	$(L_{\text{IGL}}/L_{\text{Group}})_g$	M_{HI} ($\times 10^9 M_\odot$)	D (Mpc)
(1)	(2)	(3)	(4)	(5)	(6)	(7)	(8)	(9)
NGC 5018	3	1.6	11.39	70.60	47%	41%	2.4	31.4
NGC 1533	3	1.6	14.17	3.46	12%	8%	7.7	21.0
IC 1459	9	0.3	13.10	7.17	4%	2%	22.2	28.7

Notes. Col. 1 - group name. Col. 2 and Col. 3 - number of bright galaxies in the group ($M_g < -17$) and fraction of ETGs. Col. 4 and Col. 5 - integrated magnitude and luminosity in g band of the IGL. Col. 6 and Col. 7 - fraction of intragroup light divided by the BGG luminosity and total luminosity of the group. Col. 8 - total HI mass associated to the group. Col. 9 - distance of the group used to estimate the total HI mass; for NGC 5018 by Kim et al. (1988), for NGC 1533 by Kilborn et al. (2005) and for IC 1459 by Kilborn et al. (2009).

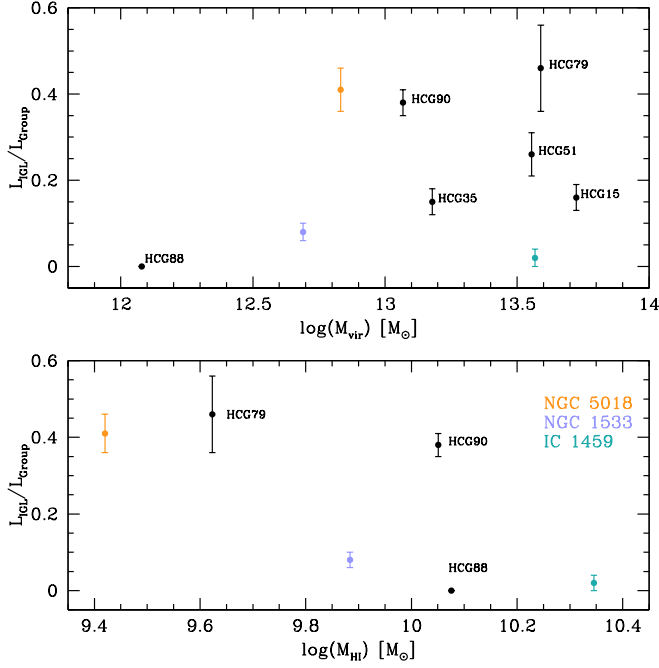


Fig. 9. Luminosity of the IGL component normalised to the total group luminosity as a function of the total HI mass of the group (lower panel) and of the virial mass of the group (top panel), for NGC 5018 group (orange), NGC 1533 triplet (mauve), IC 1459 group (teal). Values are compared with those for several Hickson Compact groups (HCGs). For HCG 79 and HCG 88 data are from Borthakur et al. (2010); Da Rocha & Mendes de Oliveira (2005); Ribeiro et al. (1998); Nishiura et al. (2000). For the remaining HCGs data are taken from Da Rocha et al. (2008); Selim & Iqbal (2008).

7. Summary and Conclusions

In this work we have presented and analysed new deep imaging data from the VEGAS survey for the galaxy group IC 1459. The VST mosaics in g , r and i bands cover the whole group extension over an area of 1×2 square degrees. We have compared the properties of this group with those of other two low density systems from VEGAS, with similar virial masses: the NGC 5018 group and the NGC 1533 triplet. The NGC 5018 and NGC 1533 groups have similar environments: they have the same number of large galaxies and of ETGs, their HI mass has the same order of magnitude, and their galaxies are closer in projection to each other. On the contrary, the IC 1459 group is a richer environment with 9 bright galaxies of which 7 are LTGs, it has a total

HI mass of $\sim 10^{10} M_\odot$, and galaxies are located in projection along a filamentary structure 2 degrees long.

This work aim at studying low-density environments, still unexplored at the faintest surface brightness levels where the stellar envelope in the galaxy outskirts and the intra-group light start to dominate. Taking advantage of the deep imaging from VEGAS, the main goal is to address the mass assembly history of the group and their members. This is done by studying *i*) the structure of the BGG outskirts, where the "tracers" of the ongoing accretion (i.e. tidal tails, stellar streams and shells) can be detected; *ii*) the azimuthally-averaged surface-brightness radial profile, in order to estimate the accreted stellar mass component; *iii*) the amount of IGL and its distribution. The main properties listed above were correlated with the HI gas mass and distribution.

The main results of this work are the following.

1. In the outskirts of IC 1459, which is the BGG of the group, we detected several LSB features in the surface brightness level $25 \leq \mu_g \leq 27$ mag arcsec $^{-2}$. They are shells, with red colours, in the NE side and two faint and bluer tails in south (see Fig. 2). All seem to be signs of interaction and accretion in the galaxy stellar halo. Same features are detected in the BGG of another group from the VEGAS sample, NGC 1533, from Cattapan et al. (2019). Differently from both of them, in the NGC 5018 group a prominent and very extended tidal tail was found, and the BGG's outskirts is characterised by several stellar streams (Spavone et al. 2018).
2. Like in NGC 5018 and NGC 1533, the azimuthally-averaged surface brightness profiles show an extended exponential envelope down to $\mu_g \sim 29$ mag/arcsec 2 and out about $9R_e$ (see Fig. 3). By fitting the light distribution, we estimate that the accreted stellar mass in this galaxy is 87%, which is similar to those derived for NGC 5018 and NGC 1533 (92% and 78%, respectively) and to those of galaxies with comparable total stellar mass in other groups or clusters of galaxies (see Fig. 7).
3. The IC 1459 group has a very low ($\sim 2\%$) fraction of IGL compared to NGC 5018 and NGC 1533, consistently with its small ETGs/LTGs ratio and the high HI amount (see Fig. 9).

The above results suggest that the three groups are in a different phase of mass assembly. The filamentary distribution of galaxies in IC 1459, where the HI gas is still associated to the 7 LTGs, and very low amount of IGL are an indication that there were few and minor interactions between the group members and the BGG, which generated the shells and tidal tails detected in the outskirts of IC 1459 (also probably related to the HI over-density observed in the same regions). According to simulations (Mancillas et al. 2019), this would have happened in the

latest 4 Gyr, which is the survival time of such a features. On the contrary, in both NGC 5018 and NGC 1533 groups, many more interactions have happened in their formation history that induced gas-depletion, by ram pressure stripping, and produced the higher IGL amount and the disturbed HI distribution which clearly traces the ongoing interaction between some group members (Cattapan et al. 2019; Spavone et al. 2018). In fact, the HI distribution is related to the environment and to the interaction history of the galaxies. Typically, in interacting or merging galaxies in groups, the HI is located along tails, streams and bridges, indicating that these structures are formed by tidal stripping (Bekki et al. 2005; Kilborn et al. 2009).

The above scenario is consistent with a different evolutionary stage of the NGC 5018 and NGC 1533 groups with respect to IC 1459: both of them have an higher ETGs/LTGs ratio with respect to that in IC 1459. A larger amount of IGL is expected for more evolved systems with higher the ETGs/LTGs ratio (Da Rocha et al. 2008). The color-magnitude diagram also confirm that NGC 5018 and NGC 1533 groups are more evolved systems than IC 1459 group, since almost all group members are approaching the red sequence, while in IC 1459 group most of the members are still in the region of active and star forming galaxies (see Fig. 6).

As concluding remark, this work shows that the structure of the outer envelope of the BCGs (i.e. the signatures of past mergers and tidal interactions), the IGL component and the HI amount and distribution may be used as indicators of the different evolutionary stage and mass assembly in galaxy groups. We plan to perform the analysis presented in this work on a larger group sample by VEGAS project in the next two years.

Acknowledgements—This work is based on visitor mode observations taken at the ESO La Silla Paranal Observatory within the VST Guaranteed Time Observations, Programme IDs 097.B-0806(B), 098.B-0208(A) and 0100.B-0168(A). The authors wish to thank the anonymous referee for his or her comments and suggestions that allowed us to greatly improve the paper. EI acknowledge financial support from the ESO inside the visitor program 2019/2020. AC, MS and EI acknowledge financial support from the VST project (P.I. P. Schipani). The VST project is a joint venture between ESO and the National Institute for Astrophysics (INAF) in Naples, Italy. RR acknowledges funding from the INAF PRIN-SKA 2017 program 1.05.01.88.04. EMC acknowledges financial support from Padua University through grants DOR1715817/17, DOR1885254/18, DOR1935272/19, and BIRD164402/16. GD acknowledges support from CONICYT project Basal AFB-170002.

References

- Amorisco, N. C. 2017, *MNRAS*, 464, 2882
- Arnaboldi, M., Ventimiglia, G., Iodice, E., Gerhard, O., & Coccato, L. 2012, *A&A*, 545, A37
- Bekki, K., Koribalski, B. S., Ryder, S. D., & Couch, W. J. 2005, *MNRAS*, 357, L21
- Bender, R., Kormendy, J., Cornell, M. E., & Fisher, D. B. 2015, *ApJ*, 807, 56
- Borthakur, S., Yun, M. S., & Verdes-Montenegro, L. 2010, *ApJ*, 710, 385
- Bower, R. G. & Balogh, M. L. 2004, in *Clusters of Galaxies: Probes of Cosmological Structure and Galaxy Evolution*, ed. J. S. Mulchaey, A. Dressler, & A. Oemler, 325
- Brough, S., Forbes, D. A., Kilborn, V. A., & Couch, W. 2006, *MNRAS*, 370, 1223
- Buta, R. 1995, *The Astrophysical Journal Supplement Series*, 96, 39
- Capaccioli, M., Spavone, M., Grado, A., et al. 2015, *A&A*, 581, A10
- Cattapan, A., Spavone, M., Iodice, E., et al. 2019, *ApJ*, 874, 130
- Contini, E., De Lucia, G., Villalobos, A., & Borgani, S. 2014, *MNRAS*, 437, 3787
- Cook, B. A., Conroy, C., Pillepich, A., Rodriguez-Gomez, V., & Hernquist, L. 2016, *ApJ*, 833, 158
- Cooper, A. P., Cole, S., Frenk, C. S., et al. 2010, *MNRAS*, 406, 744
- Cooper, A. P., D'Souza, R., Kauffmann, G., et al. 2013, *MNRAS*, 434, 3348
- Cooper, A. P., Parry, O. H., Lowing, B., Cole, S., & Frenk, C. 2015, *MNRAS*, 454, 3185
- Da Rocha, C. & Mendes de Oliveira, C. 2005, *MNRAS*, 364, 1069
- Da Rocha, C., Ziegler, B. L., & Mendes de Oliveira, C. 2008, *MNRAS*, 388, 1433
- De Lucia, G., Springel, V., White, S. D. M., Croton, D., & Kauffmann, G. 2006, *MNRAS*, 366, 499
- de Vaucouleurs, G., de Vaucouleurs, A., Corwin, Herold G., J., et al. 1991, *Third Reference Catalogue of Bright Galaxies*
- Deason, A. J., Belokurov, V., Evans, N. W., & Johnston, K. V. 2013, *ApJ*, 763, 113
- DeMaio, T., Gonzalez, A. H., Zabludoff, A., et al. 2018, *MNRAS*, 474, 3009
- Dénes, H., Kilborn, V. A., & Koribalski, B. S. 2014, *MNRAS*, 444, 667
- Donzelli, C. J., Muriel, H., & Madrid, J. P. 2011, *The Astrophysical Journal Supplement Series*, 195, 15
- D'Souza, R., Kauffman, G., Wang, J., & Vegetti, S. 2014, *MNRAS*, 443, 1433
- Duc, P.-A. 2017, in *IAU Symposium*, Vol. 321, *Formation and Evolution of Galaxy Outskirts*, ed. A. Gil de Paz, J. H. Knapen, & J. C. Lee, 180–182
- Duc, P.-A., Cuillandre, J.-C., Karabal, E., et al. 2015, *MNRAS*, 446, 120
- Eskridge, P. B., Frogel, J. A., Pogge, R. W., et al. 2002, *The Astrophysical Journal Supplement Series*, 143, 73
- Feldmeier, J., Mihos, C., Morrison, H., & Harding, P. 2004, in *American Astronomical Society Meeting Abstracts*, Vol. 205, 146.01
- Ferrarese, L., Côté, P., Cuillandre, J.-C., et al. 2012, *ApJS*, 200, 4
- Firth, P., Evstigneeva, E. A., Jones, J. B., et al. 2006, *MNRAS*, 372, 1856
- Forbes, D. A., Franx, M., & Illingworth, G. D. 1994, *ApJ*, 428, L49
- Forbes, D. A., Gannon, J., Couch, W. J., et al. 2019, *A&A*, 626, A66
- Forbes, D. A., Reitzel, D. B., & Williger, G. M. 1995, *AJ*, 109, 1576
- Franx, M. & Illingworth, G. D. 1988, *ApJ*, 327, L55
- Fujita, Y. 2004, *Publications of the Astronomical Society of Japan*, 56, 29
- Gourgoulhon, E., Chamaraux, P., & Fouque, P. 1992, *A&A*, 255, 69
- Grado, A., Capaccioli, M., Limatola, L., & Getman, F. 2012, *Memorie della Società Astronomica Italiana Supplementi*, 19, 362
- Hickson, P., Mendes de Oliveira, C., Huchra, J. P., & Palumbo, G. G. 1992, *ApJ*, 399, 353
- Huang, S., Ho, L. C., Peng, C. Y., Li, Z.-Y., & Barth, A. J. 2013, *ApJ*, 766, 47
- Iodice, E., Capaccioli, M., Grado, A., et al. 2016, *ApJ*, 820, 42
- Iodice, E., Spavone, M., Cantello, M., et al. 2017a, *ApJ*, 851, 75
- Iodice, E., Spavone, M., Capaccioli, M., et al. 2017b, *ApJ*, 839, 21
- Iodice, E., Spavone, M., Capaccioli, M., et al. 2019, *A&A*, 623, A1
- Kilborn, V. A., Forbes, D. A., Barnes, D. G., et al. 2009, *MNRAS*, 400, 1962
- Kilborn, V. A., Koribalski, B. S., Forbes, D. A., Barnes, D. G., & Musgrave, R. C. 2005, *MNRAS*, 356, 77
- Kim, D. W., Guhathakurta, P., van Gorkom, J. H., Jura, M., & Knapp, G. R. 1988, *ApJ*, 330, 684
- La Barbera, F., Ferreras, I., de Carvalho, R. R., et al. 2012, *MNRAS*, 426, 2300
- Malin, D. F. 1985, *Food for the Photometrists - Faint Galaxies Revealed*, ed. J. L. Nieto, 27
- Mancillas, B., Duc, P. A., Combes, F., et al. 2019, *arXiv e-prints*, arXiv:1909.07500
- Martel, H., Barai, P., & Brito, W. 2012, *ApJ*, 757, 48
- Mazzei, P., Marino, A., & Rampazzo, R. 2014, *ApJ*, 782, 53
- McFarland, J. P., Verdoes-Kleijn, G., Sikkema, G., et al. 2013, *Experimental Astronomy*, 35, 45
- McGee, S. L. & Balogh, M. L. 2010, *MNRAS*, 405, 2069
- Merritt, A., van Dokkum, P., Danieli, S., et al. 2016, *ApJ*, 833, 168
- Mihos, C. 2015, *IAU General Assembly*, 22, 2247903
- Mihos, J. C., Harding, P., Feldmeier, J. J., et al. 2017, *ApJ*, 834, 16
- Miles, T. A., Raychaudhury, S., Forbes, D. A., et al. 2004, *MNRAS*, 355, 785
- Monachesi, A., Gómez, F. A., Grand, R. J. J., et al. 2019, *MNRAS*, 485, 2589
- Muñoz, R. P., Eigenthaler, P., Puzia, T. H., et al. 2015, *ApJ*, 813, L15
- Nishiura, S., Murayama, T., Shimada, M., et al. 2000, *AJ*, 120, 2355
- Oosterloo, T. A., Zhang, M. L., Lucero, D. M., & Carignan, C. 2018, *arXiv e-prints*, arXiv:1803.08263
- Oser, L., Ostriker, J. P., Naab, T., Johansson, P. H., & Burkert, A. 2010, *ApJ*, 725, 2312
- Osmond, J. P. F. & Ponman, T. J. 2004, *MNRAS*, 350, 1511
- Pillepich, A., Nelson, D., Hernquist, L., et al. 2018, *MNRAS*, 475, 648
- Pop, A.-R., Pillepich, A., Amorisco, N. C., & Hernquist, L. 2018, *MNRAS*, 480, 1715
- Prichard, L. J., Vaughan, S. P., & Davies, R. L. 2019, *MNRAS*, 1293
- Purcell, C. W., Bullock, J. S., & Zentner, A. R. 2007, *ApJ*, 666, 20
- Ribeiro, A. L. B., de Carvalho, R. R., Capelato, H. V., & Zepf, S. E. 1998, *ApJ*, 497, 72
- Ricciardelli, E., Vazdekis, A., Cenarro, A. J., & Falcón-Barroso, J. 2012, *MNRAS*, 424, 172
- Rudick, C. S., Mihos, J. C., Frey, L. H., & McBride, C. K. 2009, *ApJ*, 699, 1518
- Rudick, C. S., Mihos, J. C., & McBride, C. K. 2011, *ApJ*, 732, 48

- Ryder, S. D., Purcell, G., Andersen, V., & Davis, D. 2000, in *Astronomical Society of the Pacific Conference Series*, Vol. 197, *Dynamics of Galaxies: from the Early Universe to the Present*, ed. F. Combes, G. A. Mamon, & V. Charmandaris, 405
- Ryder, S. D., Purcell, G., Davis, D., & Andersen, V. 1997, *Publications of the Astronomical Society of Australia*, 14, 81
- Saponara, J., Koribalski, B. S., Benaglia, P., & Fernández López, M. 2018, *MNRAS*, 473, 3358
- Schipani, P., Noethe, L., Arcidiacono, C., et al. 2012, *Journal of the Optical Society of America A*, 29, 1359
- Seigar, M. S., Graham, A. W., & Jerjen, H. 2007, *MNRAS*, 378, 1575
- Selim, I. & Iqbal, N. 2008, *Turkish Journal of Physics*, 32, 133
- Serra, P., Koribalski, B., Kilborn, V., et al. 2015, *MNRAS*, 452, 2680
- Sommer-Larsen, J. 2006, *MNRAS*, 369, 958
- Spavone, M., Capaccioli, M., Napolitano, N. R., et al. 2017a, *The Messenger*, 170, 34
- Spavone, M., Capaccioli, M., Napolitano, N. R., et al. 2017b, *A&A*, 603, A38
- Spavone, M., Iodice, E., Capaccioli, M., et al. 2018, *ApJ*, 864, 149
- Thilker, D. A., Bianchi, L., Meurer, G., et al. 2007, *The Astrophysical Journal Supplement Series*, 173, 538
- Tingay, S. J. & Edwards, P. G. 2015, *MNRAS*, 448, 252
- Toledo, I., Melnick, J., Selman, F., et al. 2011, *MNRAS*, 414, 602
- van Dokkum, P. G., Abraham, R., & Merritt, A. 2014, *ApJ*, 782, L24
- Vazdekis, A., Ricciardelli, E., Cenarro, A. J., et al. 2012, *MNRAS*, 424, 157
- Venhola, A., Peletier, R., Laurikainen, E., et al. 2018, *A&A*, 620, A165
- White, P. M., Bothun, G., Guerrero, M. A., West, M. J., & Barkhouse, W. A. 2003, *ApJ*, 585, 739
- Willman, B., Governato, F., Wadsley, J., & Quinn, T. 2004, *MNRAS*, 355, 159
- Wyder, T. K., Martin, D. C., Schiminovich, D., et al. 2007, *ApJS*, 173, 293
- Zibetti, S., White, S. D. M., Schneider, D. P., & Brinkmann, J. 2005, *MNRAS*, 358, 949

Appendix A: Surface Photometry of IC 1459 group

Appendix A.1: IC 5270

This late-type barred spiral galaxy is the northernmost galaxy of the group, lying at a projected distance of 37.3 from IC 1459. From the VST images (Figure B.1) there is not a clear optical counterpart for the north-northeast HI asymmetric distribution. The edge-on galaxy inclination does not allow us to investigate the stellar disk asymmetries and bar component.

Appendix A.2: IC 5269

This is a barred lenticular galaxy with an average colour ($g - r = 0.77 \pm 0.25$ mag) consistent with the predicted colour of ETGs (La Barbera et al. 2012). It is the forth most massive ($3.32 \times 10^{10} M_{\odot}$) and smallest bright galaxy ($R_{e,g} = 2.70$ kpc) galaxy of the group. From the surface brightness profiles there is a clear evidence for the bulge and stellar disk components. Its colour profile is almost flat outside of the seeing-dominated region. It does not have any associated HI (Figure B.2).

Appendix A.3: IC 5269B

This is the second closest galaxy in projection to IC 1459 (14.5). It is the second less bright, $M_g = -19.60$ mag, and less massive, $5.0 \times 10^9 M_{\odot}$, bright galaxy of the group. This galaxy is very inclined with a bluer outer regions (Figure B.3). There is an off-centre of the HI component respect to the stellar disk, that seems to be more elongated in the opposite direction. This could be due to some galaxy-galaxy or galaxy-environment interaction, providing a tidal stripping component and this gas might build-up the debris structure around IC 1459.

Appendix A.4: IC 5264

This is a peculiar, very small ($R_{e,g} = 4.05$ kpc), edge-on, early-type spiral. The average colour ($g - r = 0.79 \pm 0.06$ mag), is too red for a LTG, but this galaxy is seen in projection in the IC 1459 stellar halo. Hence this could explain that they have a similar $g - r$ average colour. From the VST images (Figure B.4), we were able to detect the warped structure of the outer stellar envelope and a dust lane in the southeaster side of the stellar disk in agreement with the HI off-centre distribution, which seems to be tangent to the outer envelope of IC 1459 in the eastern direction. Its HI component is faint and it is spread in a wide velocity range (Serra et al. 2015). It has been suggested that IC 5264 is the principal donor of HI gas around IC 1459 due to a tidal interaction (Saponara et al. 2018).

Appendix A.5: ESO 406-27

This is the bluest ($g - r = 0.34 \pm 0.20$ mag) bright galaxy of the group, and has a total stellar mass ($3.2 \times 10^9 M_{\odot}$) one order of magnitude smaller than the other galaxies except for IC 5269B. It is located on the South-West side of IC 1459, at a project distance of 19.5'. It is one of the HI brightest sources with a HI mass of $(4.6 \pm 0.9) \times 10^9 M_{\odot}$ (Serra et al. 2015). From Figure B.5, ESO 406-27 might be interacting both with IC 1459 and NGC 7418. It has a two spiral-arms pattern clearly in the direction of these galaxies, which corresponds to the HI asymmetry. However we have not enough information yet for making an hypothesis regarding the evolution/interaction scenario between IC 1459, ESO 406-27, and NGC 7418. GALEX data confirms that there are two spiral, UV-bright arms extending from north-east to southwest (Thilker et al. 2007).

Appendix A.6: NGC 7418

It is the second brightest ($M_g = -21.98$ mag), massive ($10.87 \times 10^{10} M_{\odot}$), and biggest ($R_{e,g} = 21.72$ kpc), galaxy of the group and it is at a projected distance of 34.8 from IC 1459 in the South region of the group. This late-type spiral has a very asymmetric stellar disk in the North-West direction. It has a weak optical bar, seen in the surface brightness profile rather than in the optical colour composite image (Figure B.6). It seems to be stronger in H band imaging (Eskridge et al. 2002). The spiral arms are well defined in the inner regions, becoming bluer and smoothed in the outer parts. As explored by Serra et al. (2015) and Oosterloo et al. (2018), the complex HI tidal features elongated from the North region of the group to NGC 7418 seems to be the result of the first tidal galaxy-galaxy and galaxy-environment interactions having occurred in the BGG neighbourhood.

Appendix A.7: NGC 7421

It is a late-type barred spiral with an inner resonance ring (Buta 1995). It has the smallest relative velocity ($v_{rel} = -9.59$ km s $^{-1}$) with respect to IC 1459. It is the third smallest, $R_{e,g} = 5.26$ kpc, and less massive, $2.44 \times 10^{10} M_{\odot}$, galaxy. The colour composite VST image (Figure B.7, left panel) shows the small inner bar and the South-East light asymmetries due to the spiral arms and the outer envelope of the galaxy, that are consistent with the off-centre of the HI disk. The recent study made by Serra et al. (2015) has shown that the HI asymmetry in the opposite direction of the star-forming optical disk might be the signature of ram pressure stripping. According to Dénes et al. (2014), this

galaxy is a HI-deficient galaxy, $\mathcal{M}_{\text{HI}} = (1.1 \pm 0.3) \times 10^9 \mathcal{M}_{\odot}$ (Serra et al. 2015). However according to Ryder et al. (1997) and Ryder et al. (2000), the tenuous hot intragroup medium is not able to produce a significant ram pressure stripping and hence tidal interactions might produce a couple of tails. The conclusion is that the galaxy had a previous tidal interaction, maybe with NGC 7418, which affected the stellar disk and the HI gas, and a subsequent weak ram pressure stripping, as happened for IC 5273, which dislocated the HI gas.

Appendix A.8: IC 5273

This late-type barred spiral is the third brightest galaxy of the group ($M_g = -21.59$ mag). It is the most distant galaxy in projection from IC 1459 (79:2), and it has the larger relative velocity to IC 1459 ($v_{\text{rel}} = -509 \pm 17 \text{ km s}^{-1}$). The bar is clearly visible (Figure B.8) both in the colour composite image and in the surface-brightness radial profile ($6'' \leq R \leq 40''$). The average colours are $g - r = 0.54$ mag and $g - i = 1.05$ mag, and the colour profiles have a bluer decline for $R > 3''$. It is also one of the brightest sources in ASKAP HI, $\mathcal{M}_{\text{HI}} = (5.4 \pm 1.1) \times 10^9 \mathcal{M}_{\odot}$ (Serra et al. 2015). There is an off-centre between the HI gas and stellar disk, and the HI distribution has a south-east asymmetry opposite to the direction of IC 1459. The galaxy could have suffered some interactions with the environment or from ram pressure stripping, as for NGC 7421 (Serra et al. 2015).

Appendix B: Surface photometry

For each galaxy of the IC 1459 group, we report the results of the surface photometry, from Figure B.1 to Figure B.8. The colour composite image (red channel for i band, green channel for r band, and blue channel for g band; left panel) extracted from the VST mosaic around the galaxy, with the HI map from the KAT-7 observations (cyan contours). We also report the azimuthally-averaged surface-brightness radial profile plotted in logarithmic scale as a function of the semi-major axis (middle panel), and the azimuthally-averaged extinction-corrected $g - r$, $r - i$, and $g - i$ colour profile as a function of the logarithmic semi-major axis (right panel). These plots are derived by the isophote fit from g (blue dots), r band (orange dots), and i band (red dots) VST images.

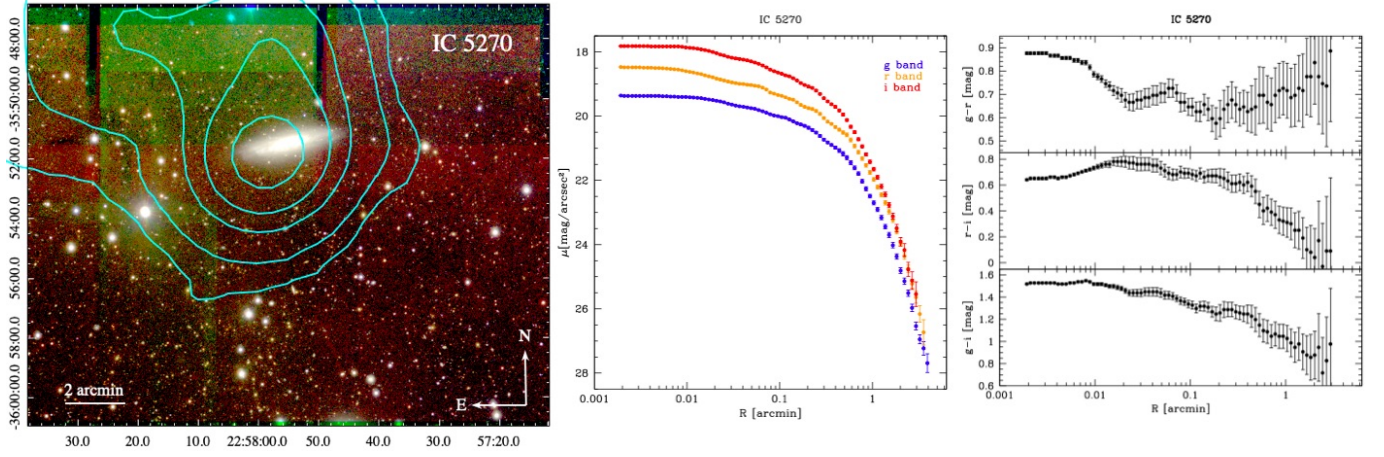


Fig. B.1. Left panel: colour composite image of IC 5270 with north at the top and east on the left. The right ascension and declination (J2000) are given in the horizontal and vertical axis of the field of view, respectively. The HI contours levels (white contours) are 1, 2.5, 7.5, 12.5, and $20 \times 10^{19} \text{ cm}^{-2}$. The white arrow indicates the direction of the BGG, IC 1459, respect with the galaxy. Middle panel: g , r , and i band azimuthally-averaged surface-brightness radial profile. Right panel: azimuthally-averaged extinction-corrected $g-r$, $r-i$, and $g-i$ colour profile.

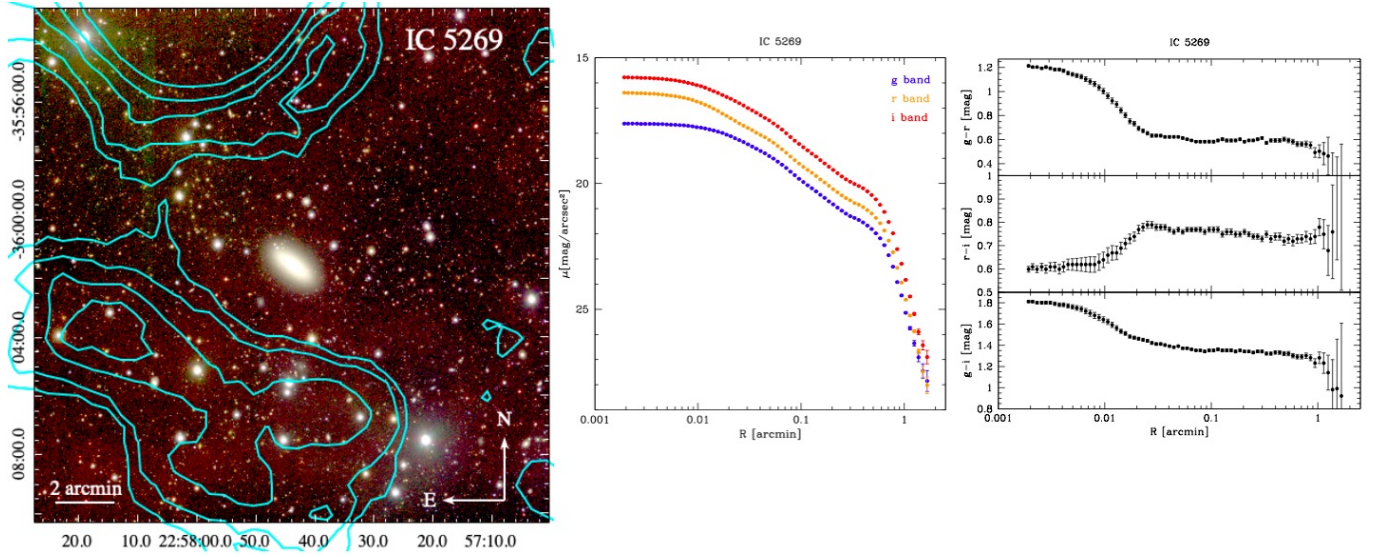


Fig. B.2. Same as Figure B.1 but for IC 5269. The HI contour levels are 0.25, 0.5, 1, 1.5, and $2.5 \times 10^{19} \text{ cm}^{-2}$.

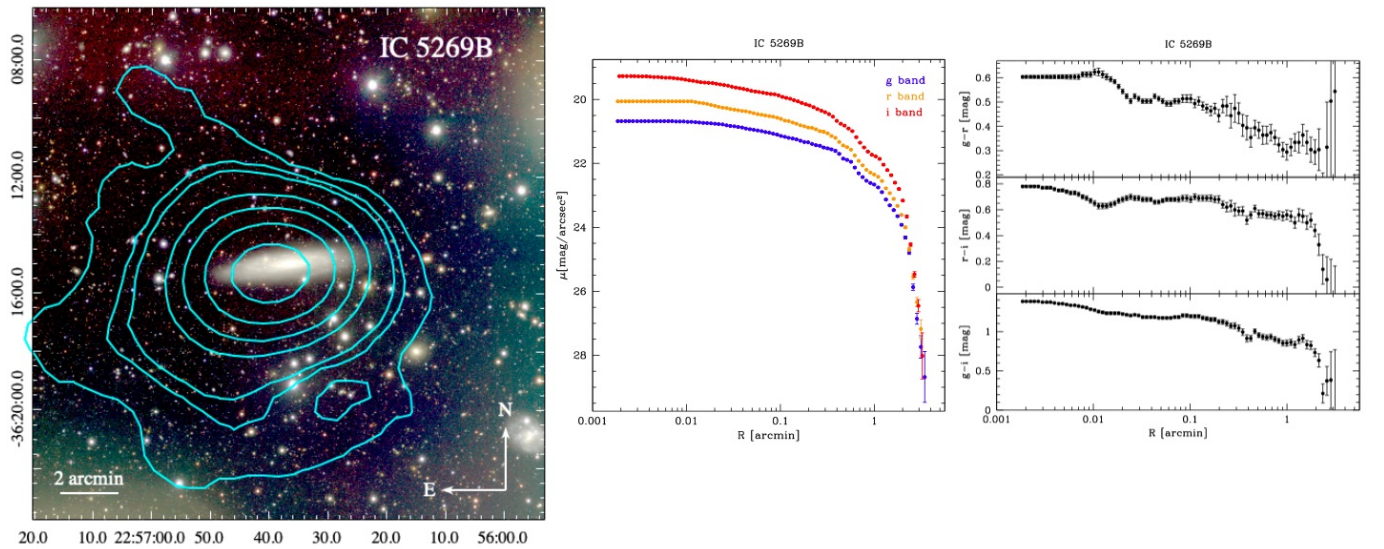


Fig. B.3. Same as Figure B.1 but for IC 5269B. The HI contour levels are 0.25, 1, 2.5, 7.5, 12.5, 20, and $30 \times 10^{19} \text{ cm}^{-2}$.

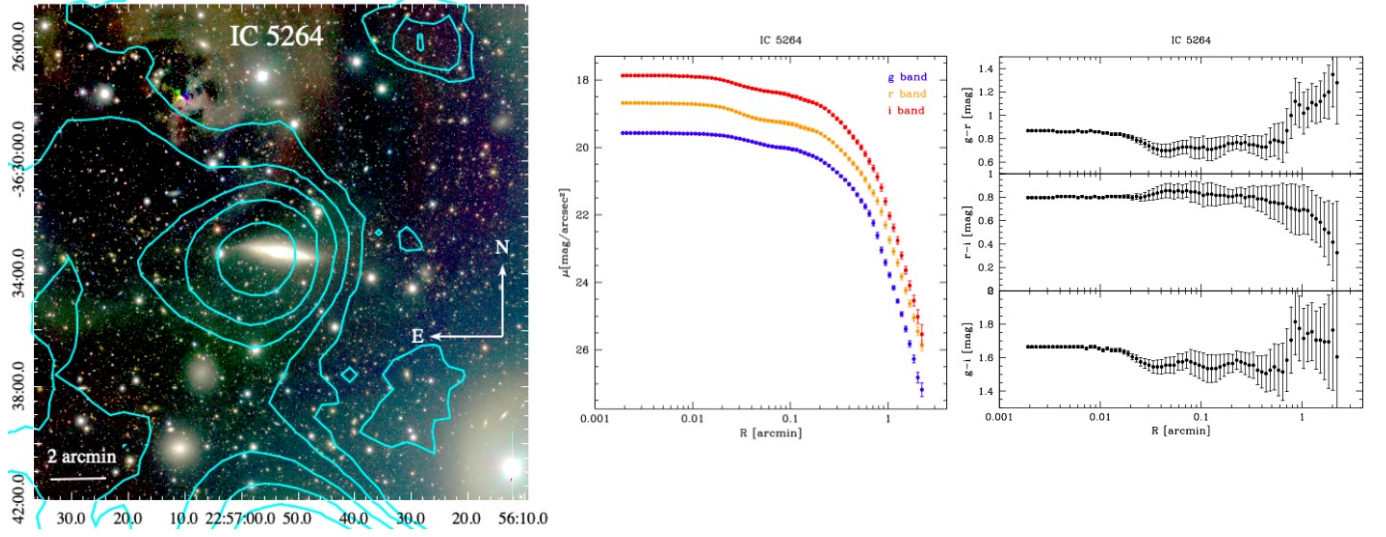


Fig. B.4. Same as Figure B.1 but for IC 5264. The HI contour levels are $0.25, 1, 2.5, 5$, and $10 \times 10^{19} \text{ cm}^{-2}$.

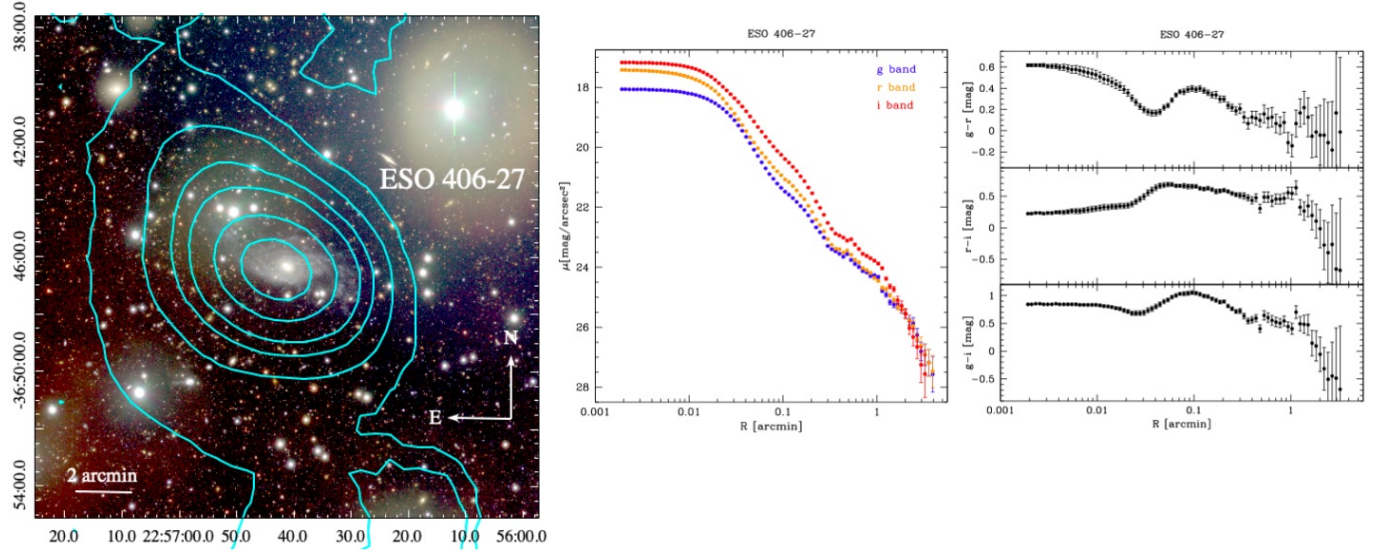


Fig. B.5. Same as Figure B.1 but for ESO 406-27. The HI contour levels are $1.5, 5, 10, 15, 25$, and $35 \times 10^{19} \text{ cm}^{-2}$.

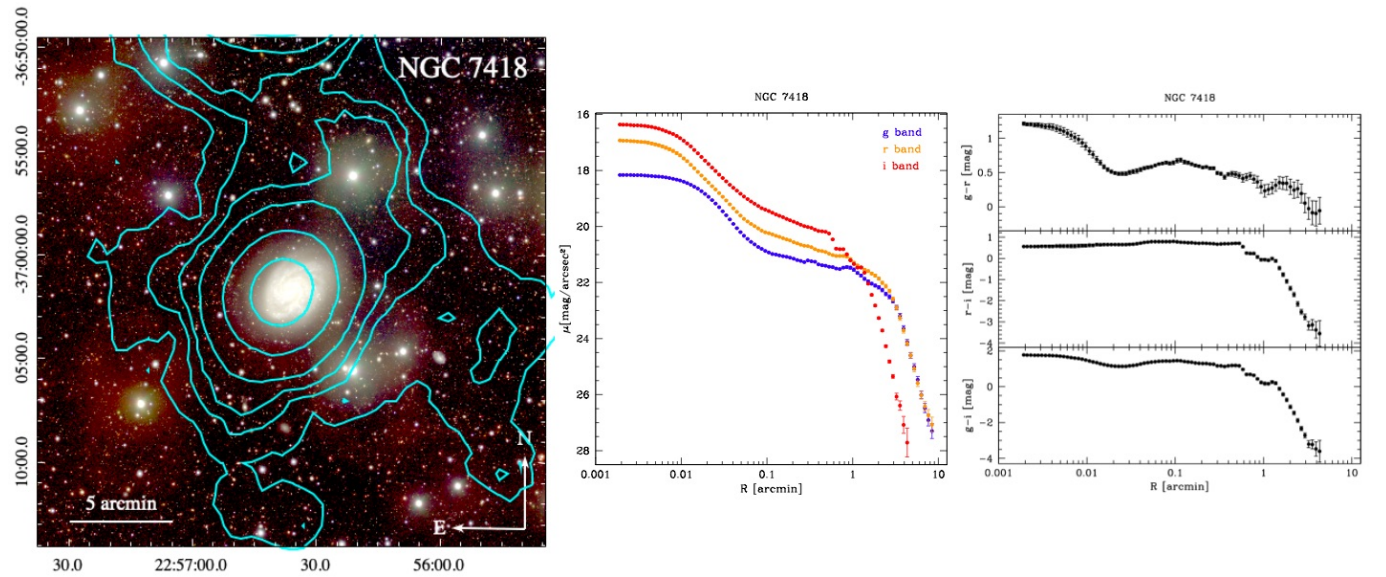


Fig. B.6. Same as Figure B.1 but for NGC 7418. The HI contour levels are $0.5, 1.5, 2.5, 5, 15$, and $35 \times 10^{19} \text{ cm}^{-2}$.

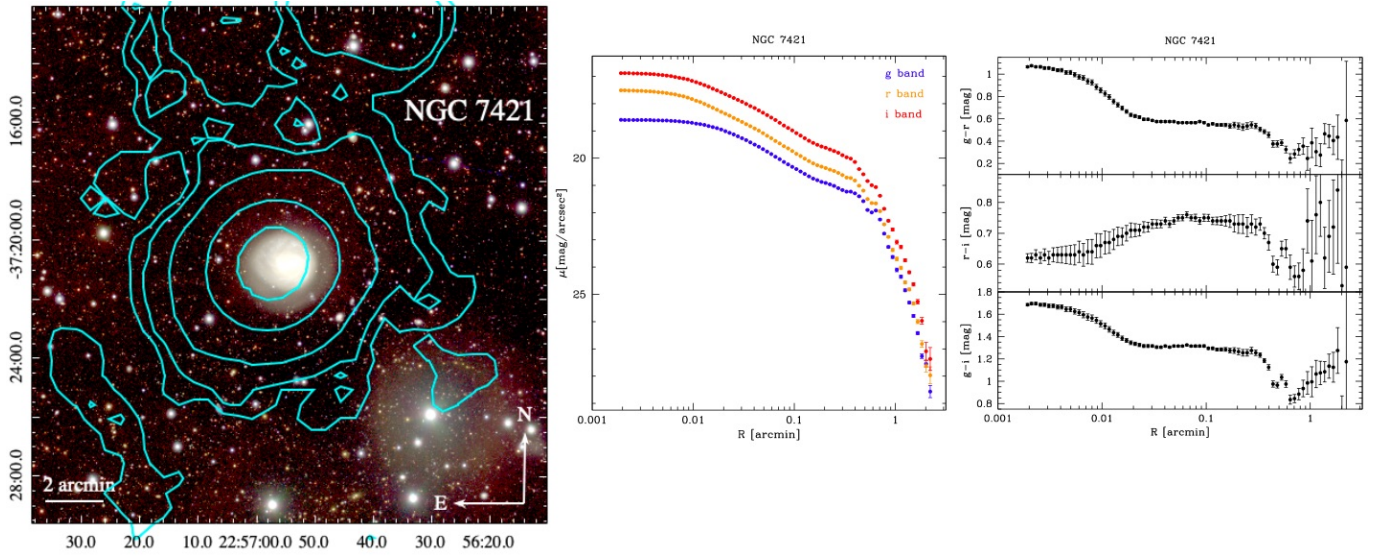


Fig. B.7. Same as Figure B.1 but for NGC 7421. The HI contour levels are $0.25, 0.5, 1.5, 5,$ and $10 \times 10^{19} \text{ cm}^{-2}$.

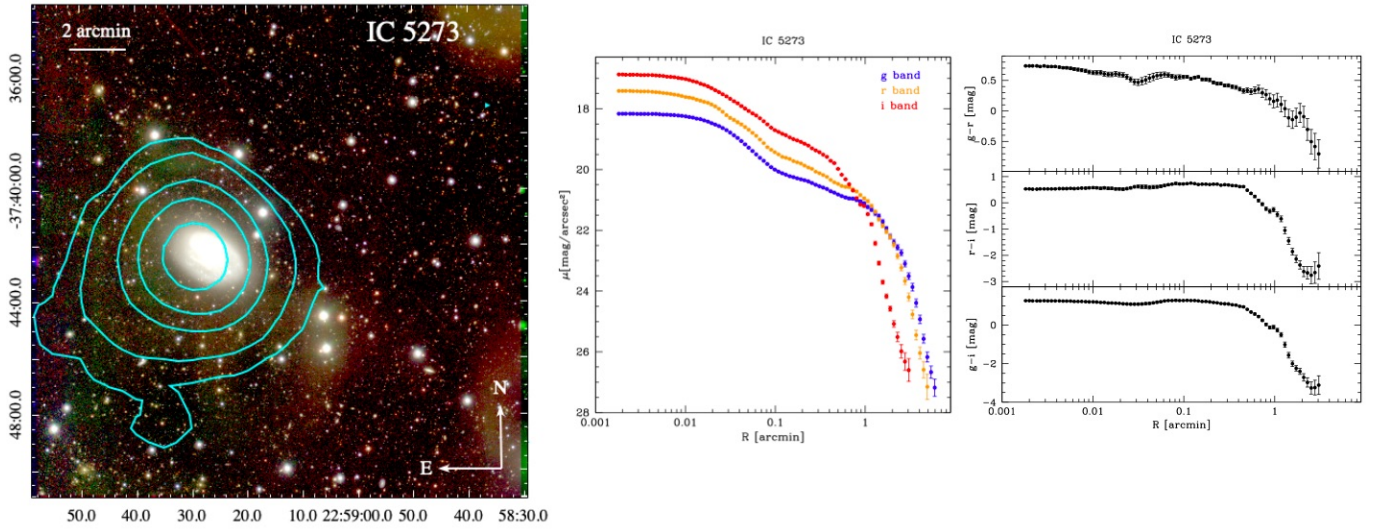


Fig. B.8. Same as Figure B.1 but for IC 5273. The HI contour levels are $1, 2.5, 7.5, 12.5,$ and $20 \times 10^{19} \text{ cm}^{-2}$.